Density functional theory modeling of cation diffusion in tetragonal bulk ZrO_2: Effects of humidity and hydrogen defect complexes on cation transport

Yueh-Lin Lee,[1,3,*] Yuhua Duan,[1,†] Dan C. Sorescu,[1] Dane Morgan,[1,5] Harry Abernathy,[2,4] Thomas Kalapos,[1,3] and Gregory Hackett[2]

[1]*National Energy Technology Laboratory, 626 Cochrans Mill Road, P.O. Box 10940, Pittsburgh, Pennsylvania 15236-0940, USA*
[2]*National Energy Technology Laboratory, 3610 Collins Ferry Road, P.O. Box 880, Morgantown, West Virginia 26507-0880, USA*
[3]*Leidos Research Support Team, 626 Cochrans Mill Road, P.O. Box 10940, Pittsburgh, Pennsylvania 15236-0940, USA*
[4]*Leidos Research Support Team, 3610 Collins Ferry Road, P.O. Box 880, Morgantown, West Virginia 26507-0880, USA*
[5]*Department of Materials Science and Engineering, University of Wisconsin–Madison, Madison, Wisconsin 53706, USA*

(Received 30 June 2020; accepted 6 January 2021; published 8 February 2021)

Density functional theory modeling was performed to determine the effect of humidity and H_2/O_2 gas pressure on the defect chemistry, hydrogen solubility and diffusivity, and on cation transport in tetragonal bulk ZrO_2, for the temperature range 400–1200 °C. The main goal of this study is to identify the stable defect complexes and hydrogen-related defect species relevant to bulk cation transport kinetics at various gas pressure, humidity, and temperature conditions, including cation diffusion via a Zr vacancy mechanism [with −4 charge, $V_{Zr}(-4)$], through an H-substituted Zr defect mechanism [via an$H$ substituted Zr defect with −3 charge, $H_{Zr}(-3)$], and via formation of fully or partially bound Schottky defect complexes (V_{Zr}-V_O and V_O-V_{Zr}-V_O). At low temperatures ($T < 500$ °C) and humidity condition of 3%, the modeling results show a 0.5–0.7-eV reduction in the apparent formation free energy of $H_{Zr}(-3)$ versus that of $V_{Zr}(-4)$ due to the attractive interaction between interstitial hydrogen and the Zr vacancy, leading to a concentration of the $H_{Zr}(-3)$ defect species that is higher than $V_{Zr}(-4)$ specie. The migration barriers of the $H_{Zr}(-3)$ versus $V_{Zr}(-4)$ are found to be comparable, i.e., 2.7 eV versus 2.4 eV for the out-of-*ab*-plane migration and 3.1 eV versus 3.0 eV for the in-*ab*-plane migration, respectively. The calculated diffusion coefficients reveal that cation diffusion in tetragonal bulk ZrO_2 will transit from the $V_{Zr}(-4)$ mechanism at high temperatures to the $H_{Zr}(-3)$ mechanism upon lowering the operating temperature and/or increasing the humidity content. The defect thermodynamic modeling results indicate that most of the stable hydrogen defect species in tetragonal bulk ZrO_2 is $H_{Zr}(-3)$, and its concentration is 4–6 orders of magnitude higher than that of H interstitial (H_{int}). Nonetheless, the most active hydrogen transport occurs via $H_{int}(+1)$ with migration barriers 0.2–0.4 eV rather than through the stable $H_{Zr}(-3)$ defect which has a larger migration barrier of 1.6 eV. At temperatures higher than 1173 K, the protonic transport rate in bulk tetragonal ZrO_2 is predicted to be several orders of magnitude higher than the bulk cation transport rate. Above 1573 K, the modeling results further predict another transition in the bulk cation transport mechanisms, $V_{Zr} \rightarrow$ fully or partially bound Schottky defects, attributed to enhanced entropic stabilization associated with oxygen vacancy formation (in the defect cluster) in equilibrium with O_2 or H_2O gas phase at the respective temperature. Overall, the results obtained highlight the importance of the coupling of the bulk cation transport kinetics with the dissolved H defect species at lower temperature and respectively, with the cation-anion vacancy clusters at higher temperature, and predict several temperature dependent mechanistic transitions for the cation transport in tetragonal bulk zirconia.

DOI: 10.1103/PhysRevResearch.3.013121

I. INTRODUCTION

Zirconia is a technologically important material for energy, environmental, electronic, sensor, and biomedical applications [1]. Understanding the factors governing compositional and microstructural changes in zirconia and their interfaces during operation is a critical aspect to the material's performance and the durability of the associated devices [2,3]. In many phenomenological degradation processes such as microstructure and compositional evolution, aging, grain growth, creep, and failure of the zirconia or its doped materials, cation transport has been identified as one of the major factors controlling the associated kinetics [4–7]. Nevertheless, the requirements for zirconia operation can span a wide range of temperature and gas pressures in applications such as solid oxide fuel/electrolysis cells, thermal barrier coatings, gas sensors, oxide scales of fuel cladding materials in nuclear reactors, etc. Fundamental mechanistic understanding is still insufficient to describe the experimental cation

*Yueh-Lin.Lee@netl.doe.gov
†Yuhua.Duan@netl.doe.gov

diffusivities in zirconia and its interfaces under various operating conditions, including their dependencies on temperature (T), partial pressure of oxygen [$P(O_2)$] and hydrogen [$P(H_2)$], and the effect of humidity [$P(H_2O)$] [1,8–10]. Several experimental studies have been reported for the bulk cation diffusivities of zirconia or yttria stabilized zirconia (YSZ), and their temperature dependencies [4,11]. In these studies, the experimentally determined cation diffusion coefficients were typically measured in the temperature range 1200–2000 °C, higher than the usual operating range of the devices. For the cation transport kinetics under typical operating temperature and gas pressure conditions, kinetic values are typically extrapolated from higher temperature measurements through the assumption of an Arrhenius-type behavior, but the accuracy of such an extrapolation scheme remains uncertain. Moreover, the effect of humidity on the cation transport was rarely addressed in the previous studies.

In this work, the cation transport mechanisms and their migration barriers in bulk tetragonal ZrO_2 were investigated within the temperature range 400–1200 °C and under various H_2/O_2 gaseous pressure and humidity conditions based on density functional theory (DFT) calculations. In addition to the cation transport carrier concentration obtained from *ab initio* thermodynamics analysis, the activation barriers for cation migration were also determined. This approach allows to evaluate the rates of bulk cation diffusion for key defect reactions and cation migration mechanisms in tetragonal ZrO_2, thereby providing insight into the cation transport kinetics. While the bulk cation diffusion rate is considered to be lower than diffusion through microstructural imperfections such as grain boundaries, dislocation, cracks, etc. [12], understanding the bulk defect chemistry and transport mechanisms is a prerequisite for further investigations, interpretations, and modeling of the interfacial defect and transport of various defined interfacial structures. Several possible bulk cation diffusion pathways have been proposed in previous studies [5,13–15], but to the authors' best knowledge, there is no study performed to date on modeling the cation transport in the presence of hydrogen defects under different O_2/H_2 gas and humidity conditions. The main goals of this study are to employ first principles DFT calculations to determine the effect of humidity, gas pressure, and temperature upon the bulk defect chemistry and cation transport in tetragonal ZrO_2 and to identify the stable hydrogen-related defect species and the factors potentially causing non-Arrhenius-type bulk cation transport kinetics. As a first step and given the configurational complexity of placing Y and oxygen vacancies in the yttria stabilized zirconia, this work focuses on the modeling of defect equilibria, cation diffusivities, and hydrogen transport in the bulk tetragonal ZrO_2 without doping, with additional analysis performed to assess Zr diffusivities in 3-mol % YSZ under the assumption of Y-doping independent Schottky defect formation. This work is organized as follows: Section II describes the computational modeling approaches, Sec. III discusses the bulk defect chemistry versus $P(O_2)$, $P(H_2)$, $P(H_2O)$, and temperature, Sec. IV summarizes the theoretical results of the cation migration mechanisms, the corresponding barriers, and the calculated cation diffusion coefficients in bulk tetragonal ZrO_2. Section V contains the summary and conclusions of this work.

II. COMPUTATIONAL MODELING APPROACHES

A. Density functional theory modeling of the point defect formation and migration

Spin-polarized DFT calculations were performed with the Vienna *Ab initio* Simulation Package [16,17] (VASP) using the projector-augmented plane-wave (PAW) method [18]. Exchange correlation is treated using the Perdew-Burke-Ernzerhof [19] (PBE) generalized gradient approximation (GGA). A plane wave energy cutoff of 520 eV and a Monkhorst-Pack [20] k-point mesh equivalent to $8 \times 8 \times 8$ for the primitive tetragonal unit cell were used to sample the Brillouin zone. The perfect (undefective) bulk tetragonal ZrO_2 supercells with lattice constants of $2\sqrt{2}\mathbf{a} \times 2\sqrt{2}\mathbf{a} \times 3\mathbf{c}$ were first fully relaxed, and then the supercell lattice parameters were fixed for all the defect and migration barrier calculations [15].

For the defect calculations, relaxation of the atomic positions was conducted until Hellmann-Feynman forces were below 1 meV $Å^{-1}$. Formation energies for perfect (undefective) bulk and for point defects were determined using the PyCDT module [21] based on the open-source PYTHON Materials Genomics (Pymatgen) software and the Materials Project database [22].

To correct for the long-range Coulomb interactions of the charged defects in the finite-size periodic supercells [23,24], the electrostatic correction method proposed by Kumagai *et al.* [25], which takes into account the anisotropic long-range Coulomb interactions, was applied to calculate the defect formation energies. To account for the band-gap underestimation in insulating materials calculated with the PBE functional, which may cause errors in the predicted defect levels within the band gap [26–28], a band-edge correction was applied to shift the conduction-band minimum and the valence-band maximum to be equal to those calculated using the HSE06 hybrid functional [29], by aligning their averaged bulk electrostatic potentials [27]. The calculated band edges referenced to the averaged bulk potential is provided in Table S1 of the Supplemental Material (SM) [30]. A list of the point defect species together with their various charge states and the corresponding acronyms are summarized in Table I while a pictorial view of different defect configurations of the H-defect complexes at various charge states are provided in Figs. S1–S3 of the SM. The band-edge correction was consistently applied to the results obtained from the PyCDT module of Pymatgen. Cation migration barriers for different vacancy and vacancy complexes [15,31] were obtained using the climbing image nudged-elastic-band method (cNEB) [32], based on the most stable defect charge state taken from the defect model solution for the specified operting conditions. It is assumed that the considered ionic migration does not involve change of the defect charge state in the transition states. More details of the DFT methods and defect calculations are provided in the SM.

B. *Ab initio* thermodynamic approach

The formalism of the *ab initio* thermodynamic analysis adopted from Ref. [33] is utilized in this study to obtain the formation free energies for the defect species at

TABLE I. The list of the point defect species investigated in this work together with the corresponding acronyms. Pictorial views of the $H_{\rm int}$, $H_{\rm O}$, $H_{\rm Zr}$, $2H_{\rm Zr}$, $3H_{\rm Zr}$, and $4H_{\rm Zr}$ defects in various charged states are provided in Figs. S1–S3 of the SM.

	Acronym	Defect charge states (indicated in parentheses) investigated in this work
Zr vacancy	$V_{\rm Zr}$	$V_{\rm Zr}(0)$, $V_{\rm Zr}(-1)$, $V_{\rm Zr}(-2)$, $V_{\rm Zr}(-3)$, $V_{\rm Zr}(-4)$
O vacancy	$V_{\rm O}$	$V_{\rm O}(+2)$, $V_{\rm O}(+1)$, $V_{\rm O}(0)$, $V_{\rm O}(-1)$, $V_{\rm O}(-2)$
H interstitial	$H_{\rm int}$	$H_{\rm int}(-1)$, $H_{\rm int}(0)$, $H_{\rm int}(+1)$
H substitution on the O lattice	$H_{\rm O}$	$H_{\rm O}(-1)$, $H_{\rm O}(0)$, $H_{\rm O}(+1)$
H substitution on the Zr lattice	$H_{\rm Zr}$	$H_{\rm Zr}(0)$, $H_{\rm Zr}(-1)$, $H_{\rm Zr}(-2)$, $H_{\rm Zr}(-3)$
$2H$ substitution on the Zr lattice	$2H_{\rm Zr}$	$2H_{\rm Zr}(0)$, $2H_{\rm Zr}(-1)$, $2H_{\rm Zr}(-2)$
$3H$ substitution on the Zr lattice	$3H_{\rm Zr}$	$3H_{\rm Zr}(0)$, $3H_{\rm Zr}(-1)$
$4H$ substitution on the Zr lattice	$4H_{\rm Zr}$	$4H_{\rm Zr}(0)$
Electron	e'	$e(-1)$
Hole	$h^{\bullet}$	$h(+1)$

T = 673–1473 K and at selected $P(O_2)$, $P(H_2O)$, and $P(H_2)$ conditions. While the chemical potentials of O and H can be defined by $P(O_2)$, $P(H_2)$, $P(H_2O)$, and T, only two gas partial pressures among the set of three gas species, O_2, H_2, and H_2O, are needed to determine the set of O and H chemical potentials at selected thermodynamic conditions. In order to determine the humidity effects on the defect thermodynamics and cation transport, in this work we specify the operating conditions by using $P(O_2)$ and $P(H_2O)$ [$P(O_2)$/$P(H_2O)$] or with $P(H_2)$ and $P(H_2O)$ [$P(H_2)$/$P(H_2O)$] at a given T. In Table S2 of the SM, the corresponding $P(H_2)$ at the specified T, $P(O_2)$, and $P(H_2O)$ conditions, as well as the corresponding $P(O_2)$ at the specified T, $P(H_2)$, and $P(H_2O)$ conditions, are summarized. The $P(H_2)$/$P(H_2O)$ conditions in this work were selected to be representative for applications such as solid oxide fuel cell (SOFC) anode or material synthesis.

The thermodynamic properties within lattice harmonic approximation for the bulk oxide with and without point defects were evaluated using the PHONOPY package [34]. In this work, both the defect formation energy at 0 K and the vibrational free-energy contribution to the defect formation are simulated using the $2\sqrt{2}a \times 2\sqrt{2}a \times 3c$ (288-atom) supercells. The vibrational free-energy terms were evaluated using first principles DFT phonon calculations within harmonic approximation and were used to determine the chemical potential of μ_{Zr} as a function of T and gas pressure according to expression

$$\mu_{\rm Zr} = E_{\rm DFT}(ZrO_2) + G^{\rm vib}{}_{ZrO_2}(T) - 2\mu_{\rm o}, \qquad (1)$$

where $E_{\rm DFT}(ZrO_2)$ is the calculated total energy of the bulk tetragonal ZrO_2 per formula unit, μ_O is the chemical potential of oxygen at a specified T and gas pressure condition as defined in Eq. (S3) of the SM, and $G^{\rm vib}_{ZrO_2}(T)$ is the vibrational free-energy of the perfect bulk tetragonal ZrO_2 at a given T, obtained from the PHONOPY package [34]. The vibrational free-energy contribution to the defect formation is defined as the free-energy difference between the defect containing supercell and the perfect bulk supercell under the harmonic lattice approximation, i.e., $G^{\rm vib}_{\rm defect}(X^q) - G^{\rm vib}_{\rm perf}[{\rm bulk}]$, where $G^{\rm vib}_{\rm defect}(X^q)$ is the harmonic vibrational free energy of a defect containing supercell for a defect X in charge state q and $G^{\rm vib}_{\rm perf}[{\rm bulk}]$ is the vibrational free energy of the bulk supercell. The quasiharmonic and anharmonic free-energy terms are neglected in this study. Further details of the *ab initio* thermodynamic approaches and of the bulk defect model used in this study are provided in the SM.

C. Vibrational free-energy contribution to the defect formation

The thermodynamic analysis of the point defects and H-related defect species revealed a substantial supercell size dependence of the defect formation energies on vibrational free-energy contributions, particularly in the regime of high temperatures. Specifically, upon increasing the supercell size a difference of at least 0.3 eV in the vibrational free energies of Zr vacancy ($V_{\rm Zr}$) and respectively for H-substituted Zr defect formation relative to the corresponding undefective bulk vibrational free energy was found to exist at T = 1000 K. This difference further increases at even higher temperatures, as shown in Fig. 1. The observed supercell size dependence of vibrational contribution to defect formation free energy indicates that standard $2\boldsymbol{a} \times 2\boldsymbol{a} \times 2\boldsymbol{c}$ (96-atom) supercells, generally used for calculating vibrational free energy of bulk tetragonal zirconia with point defects, is insufficiently large to represent adequately the case of defective tetragonal ZrO_2 at low defect concentrations, particularly in the regime of high temperatures. In this work, the $2\sqrt{2}\boldsymbol{a} \times 2\sqrt{2}\boldsymbol{a} \times 3\boldsymbol{c}$ (288-atom) supercell was consistently used for both the charged defect analysis and the lattice dynamics simulations. The difference in the vibrational free-energy contributions between the $2\sqrt{2}\boldsymbol{a} \times 2\sqrt{2}\boldsymbol{a} \times 3\boldsymbol{c}$ (288-atom) supercells and the largest $4a \times 4a \times 4c$ (768-atom) supercells is within 0.12 eV per defect at T = 1500 K. For the defect species included in this work, the vibrational free-energy contributions to the defect formation given by the difference between vibrational free energy of a defect containing supercell [$G^{\rm vib}_{\rm defect}(X^q)$] and that of the perfect bulk supercell ($G^{\rm vib}_{\rm perf}$[bulk]), as defined in Eq. (S1) of the SM, are summarized in Fig. 2. From this figure it can be seen that the vibrational free-energy contributions of the hydrogen defect complexes are larger and more positive than the vibrational free-energy contributions of the hydrogen-free point defects. For example, the spacing of the y-axis intercepts shown in Fig. 2(a) suggest that the zero point energy of

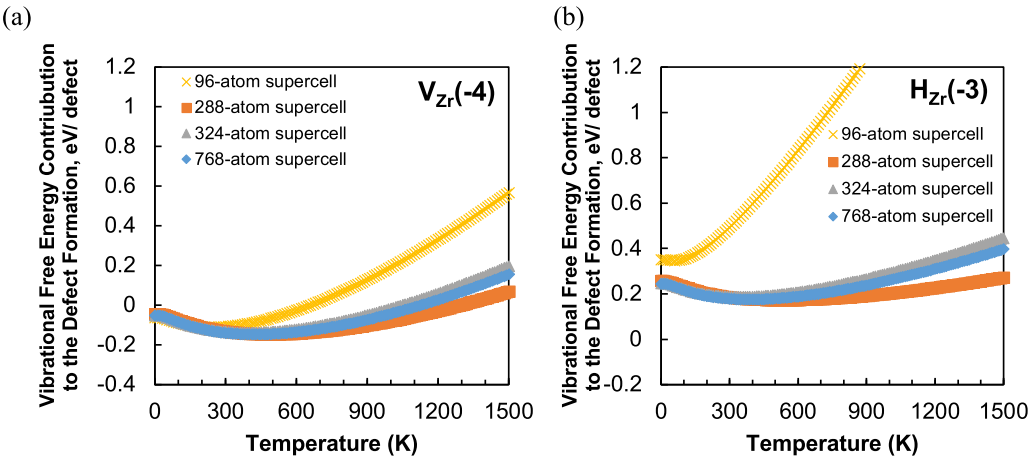

FIG. 1. The calculated vibrational free-energy contribution to the defect formation as a function of temperature for (a) Zr vacancy [$V_{Zr}(-4)$] and (b) H substitution on Zr [$H_{Zr}(-3)$]. The numbers in the parentheses correspond to the defect charge states. The orange, grey, and blue lines are results obtained using $2\sqrt{2}\boldsymbol{a} \times 2\sqrt{2}\boldsymbol{a} \times 3\boldsymbol{c}$ (288-atom), $3\boldsymbol{a} \times 3\boldsymbol{a} \times 3\boldsymbol{c}$ (324-atom), and $4\boldsymbol{a} \times 4\boldsymbol{a} \times 4\boldsymbol{c}$ (768-atom) supercells respectively, whereas the yellow line and the cross points are results obtained from the $2\boldsymbol{a} \times 2\boldsymbol{a} \times 2\boldsymbol{c}$ (96-atom) supercells.

$V_{Zr}(-4)$, $H_{Zr}(-3)$, $2H_{Zr}(-2)$, $3H_{Zr}(-1)$, and $4H_{Zr}(0)$ scales with the number of hydrogen in the point defects, and the vibrational free-energy contributions to the defect formation increase with the increasing number of H in the point defect. Therefore, the results of Fig. 2 suggest that formation of bonding associated with hydrogen in the hydrogen defect complexes leads to positive vibrational free-energy contribution to the defect formation, and can be up to +0.6–1.2 eV for the $2H_{Zr}(-2)$, $3H_{Zr}(-1)$, and $4H_{Zr}(0)$ defects already at $T = 0$ K. All the obtained vibrational free-energy contributions summarized in Fig. 2 are incorporated into the defect model for the solution of the point defect concentration at specified conditions.

It is noted that formation of the OH defect species can be important for the hydration reaction, particularly for the oxide materials containing substantial oxygen vacancy content (such

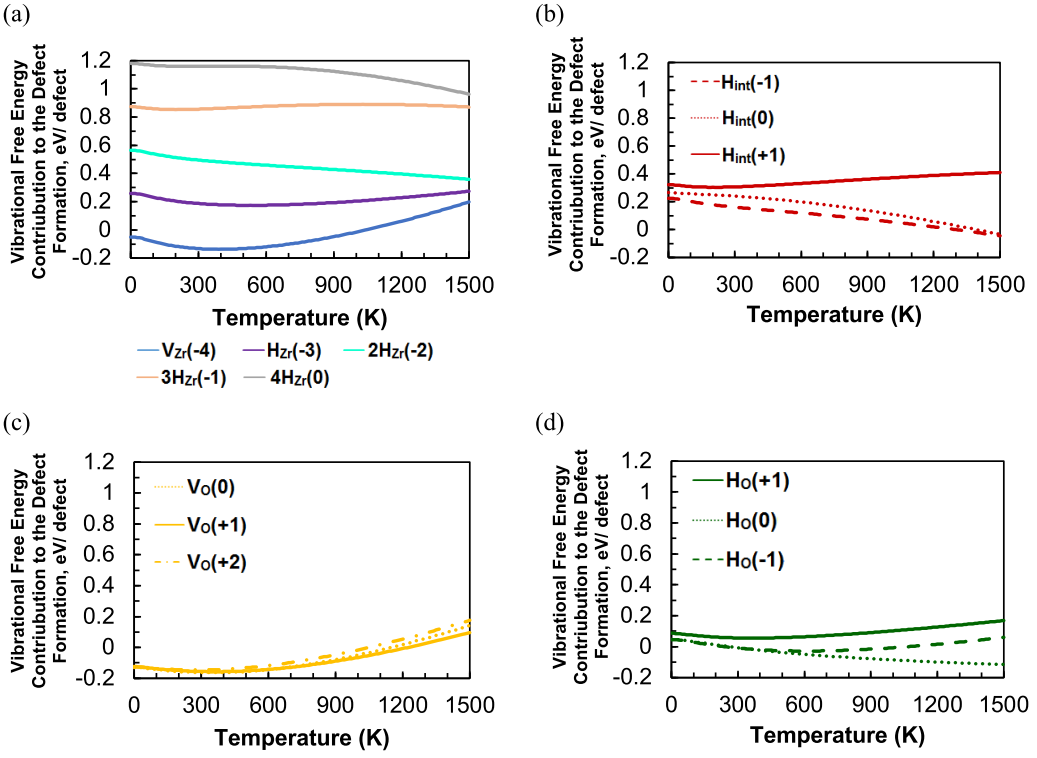

FIG. 2. The calculated vibrational free-energy contribution to the defect formation energy using $2\sqrt{2}\boldsymbol{a} \times 2\sqrt{2}\boldsymbol{a} \times 3\boldsymbol{c}$ (288-atom) supercells for (a) $V_{Zr}(-4)$ (blue line), $H_{Zr}(-3)$ (purple line), $2H_{Zr}(-2)$ (light blue line), $3H_{Zr}(-1)$ (orange line), and $4H_{Zr}(0)$ (grey line); (b) $H_{int}(-1)$ (red dashed line), $H_{int}(0)$ (red dotted line), and $H_{int}(+1)$ (red solid line); (c) $V_O(0)$ (yellow dotted line), $V_O(+1)$ (yellow solid line), and $V_O(+2)$ (yellow dotted dashed line); (d) $H_O(+1)$ (green solid line), $H_O(0)$ (green dotted line), and $H_O(-1)$ (green dashed line).

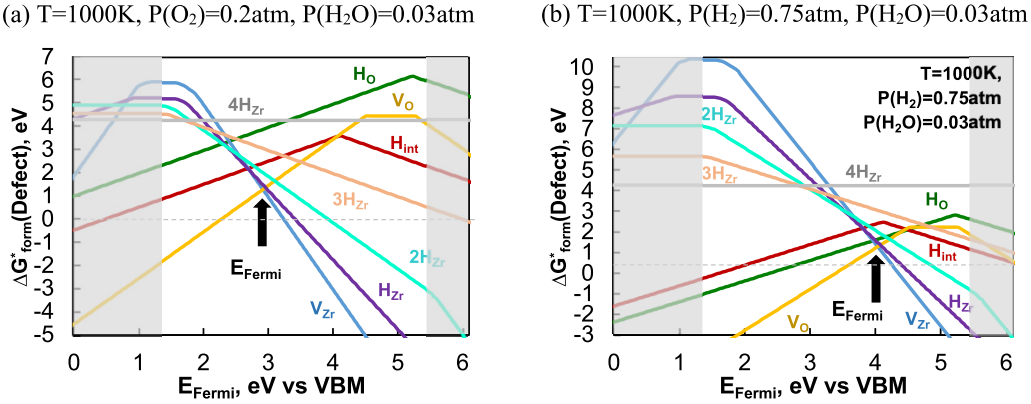

FIG. 3. The defect formation free energy, ΔG_{form}(Defect), as a function of the Fermi level (E_{Fermi}) relative to the valence-band maximum (VBM) for the bulk tetragonal ZrO_2 at the following conditions: (a) $T = 1000$ K, $P(O_2) = 0.2$ atm, and $P(H_2O) = 0.03$ atm; (b) $T = 1000$ K, $P(H_2) = 0.75$ atm, and $P(H_2O) = 0.03$ atm. It is noted that the VBM (CBM) calculated at the PBE level is shifted to the HSE06 VBM (CBM) edge after aligning the averaged bulk potentials obtained using the two functionals. The white region indicates the calculated PBE band gap with the Fermi-level range extended beyond the PBE band edge (grey regions), in order to restore the HSE06 band gap (6.1 eV versus the PBE gap of 4.2 eV). The point defect species included in the plots correspond to V_O (yellow), V_{Zr} (blue), H_{int} (red), H_O (green), H_{Zr} (purple), $2H_{Zr}$ (light blue), $3H_{Zr}$ (orange), and $4H_{Zr}$ (grey). The self-consistent Fermi level in each plot is indicated by the black arrow.

as YSZ, acceptor doped $BaZrO_3$). Recent modeling studies have also shown the impact of the phonons on the hydration and defect thermodynamics of undoped and acceptor doped $BaZrO_3$ [35,36]. In this work, the reference state for all the point defect calculations was taken to correspond to the perfect bulk tetragonal ZrO_2. In this scenario, the OH defect species can be in the form of an OH interstitial defect or an Hint defect bound with a lattice oxygen. The OH interstitial defect is energetically unfavorable to form in the closed-packed fluorite structure and is not considered in this work. On the other hand, the OH defect species in the form of an H_{int} defect bound with a lattice oxygen is considered to be in the charge state of $+1$, i.e., $H_{\text{int}}(+1)$, where the O-H bond distance is about 1 Å in the relaxed defect configuration. Since the H_{int} defect has already been taken into consideration as a defect species in the defect model, the OH defect species will not be separately discussed below to avoid double counting.

III. BULK DEFECT THERMODYNAMICS

In this section, the bulk defect chemistry of tetragonal ZrO_2 as a function of $P(O_2) - P(H_2O)$, $P(H_2) - P(H_2O)$, and temperature will be discussed. The defect model, which solves the point defect concentrations normalized as per lattice site (hereafter point defect concentration means point defect concentration normalized as per lattice site) and charge concentrations normalized as per formula unit (hereafter charge concentration means charge concentration normalized as per formula unit) at specified gas pressure and temperature conditions, is derived based on a first principles charged defect analysis [23,24] and the *ab initio* thermodynamic approach described in Sec. II. The results obtained provide guidance to the concentration of point defects, charge, and H-related defect species in bulk ZrO_2, in response to the change of temperature, gas pressure, and humidity.

A. Point defect energetics in bulk tetragonal ZrO_2 versus $P(O_2)/P(H_2O)$ and versus $P(H_2)/P(H_2O)$

Figure 3 shows the calculated defect formation free energies [denoted as ΔG_{form}(Defect)] as a function of the Fermi level (E_{Fermi}) expressed relative to the valence-band maximum (VBM) in bulk tetragonal ZrO_2, at $T = 1000$ K and specified gas pressure conditions. The calculated defect formation energies versus E_{Fermi} of all point defect species obtained directly from the DFT modeling are provided in Fig. S4 of the SM. By including the gas phase thermodynamics [33,37] and the solid phase vibrational free-energy terms, the point defect stability under various temperature and gas pressure conditions can be examined. The $P(O_2)/P(H_2O)$ and $P(H_2)/P(H_2O)$ conditions in this work were selected considering their relevance for ZrO_2 to be used in high temperature devices under oxygen rich and hydrogen rich conditions such as a SOFC electrode under open circuit conditions (note that heavily acceptor doped ZrO_2 is practically used in the SOFC instead of the undoped ZrO_2), thermal barrier coatings, gas sensors, and oxide scales of fuel cladding materials in nuclear reactors.

The self-consistent E_{Fermi} obtained from the defect model upon imposing the charge neutrality constraint is indicated by black arrows in both panels of Fig. 3. It can be seen that the defect analysis captures the Fermi level shift when going from the more oxidized condition of $P(O_2) = 0.2$ atm to the more reduced condition of $P(H_2) = 0.75$ atm at $T = 1000$ K and $P(H_2O) = 0.03$ atm, which is associated with the coupling between the electron chemical potential and the point defect stability upon varying the gas phase chemical potential for the solid oxides. The charge state of each point defect can be also identified by analyzing the slope of the ΔG_{form}(Defect) versus E_{Fermi}. Under the condition of $P(H_2O) = 0.03$ atm at $T = 1000$ K, it can be seen that at the self-consistent E_{Fermi}, the charge neutrality requirement is fulfilled mainly by the charged ionic defect species (with opposite charges) in the insulating tetragonal ZrO_2, i.e., the negatively charged

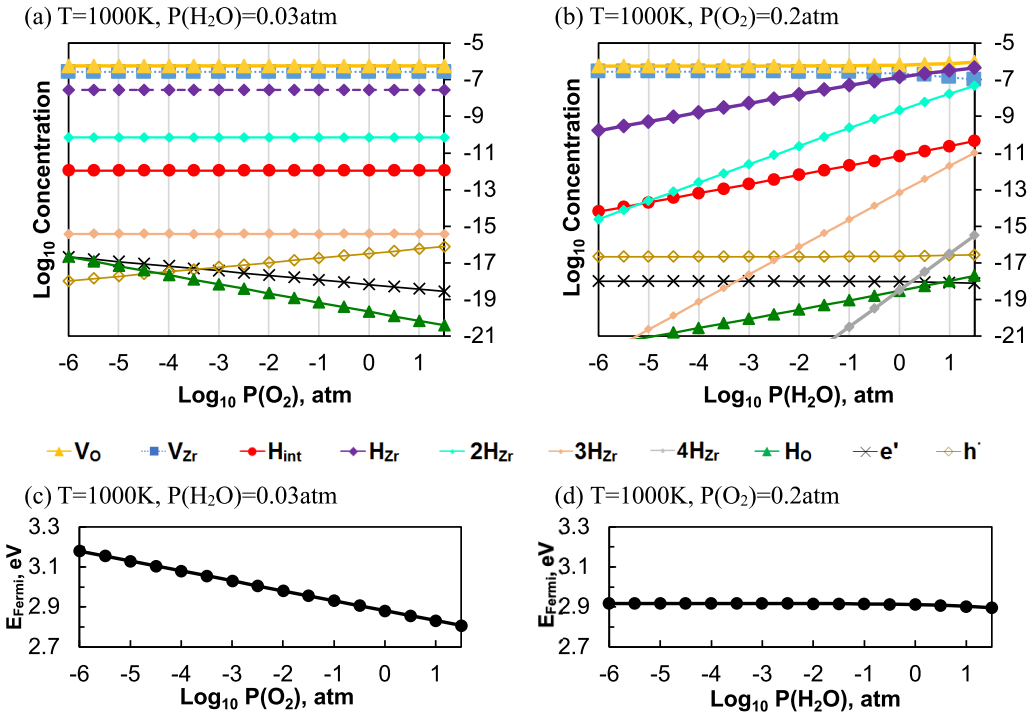

FIG. 4. (a) Concentration of the defect species versus $P(O_2)$ obtained from the defect model for the condition of $T = 1000$ K, $P(H_2O) = 0.03$ atm. (b) The concentration of the defect species versus $P(H_2O)$ obtained from the defect model for the condition of $T = 1000$ K, $P(O_2) = 0.2$ atm. The point defect species included in these plots are V_O (yellow triangle), V_{Zr} (blue squares), H_{int} (red circles), H_{Zr} (purple diamonds), $2H_{Zr}$ (light blue small diamonds), $3H_{Zr}$ (orange small diamonds), $4H_{Zr}$ (grey small diamonds), electron (black crosses, e'), and hole (grey empty diamonds, $h^{\bullet}$). The corresponding Fermi levels at varying gas pressure conditions as represented in (a) and (b) are provided in (c) and (d), respectively.

$V_{Zr}(-4)$ is compensated by $V_O(+2)$ and $H_{int}(+1)$. The closeness in stabilities between the $V_{Zr}(-4)$ and $H_{Zr}(-3)$ defect species as well as the $V_O(+2)$ and $H_{int}(+1)$ species at the self-consistent E_{Fermi} also indicates that the H-related defect species in the defect thermodynamics cannot be neglected in the case of $P(H_2O)$ larger than or equal to 0.03 atm. The defect modeling results obtained above highlight the importance of the H-related defects which may be formed under increased humidity conditions with direct influence on the observed material degradation upon increasing humidity content.

B. Point defect concentration versus $P(O_2)/P(H_2O)$ at $T = 1000$ K

For the bulk tetragonal ZrO_2, the defect concentration as a function of $P(O_2)$ under a fixed $P(H_2O)$ of 0.03 atm and at $T = 1000$ K was obtained from the bulk defect model and is provided in Fig. 4(a) while the results corresponding to $P(H_2O)$ variations under a fixed $P(O_2)$ of 0.2 atm are shown in Fig. 4(b). The corresponding intrinsic Fermi level within the band gap at varying gas pressure conditions is illustrated in Figs. 4(c) and 4(d). Details of the ΔG^*_{form}(Defect) versus E_{Fermi} plots at varying $P(O_2)$ and under a fixed $P(H_2O) = 0.03$ atm, and respectively at varying $P(H_2O)$ under a fixed $P(O_2) = 0.2$ atm are included in Fig. S5 of the SM.

As shown in Fig. 4(a), at a fixed $P(H_2O) = 0.03$ atm, the majority of the point defects are $V_O(+2)$ and $V_{Zr}(-4)$, and their concentrations are also shown to be independent of $P(O_2)$, which indicate that Schottky disorder is prevailing in the modeled defect equilibria for undoped tetragonal ZrO_2. Under these conditions the charge neutrality of the material is fulfilled by maintaining the same stoichiometry at varying charge concentrations [38]. The concentration of hydrogen defect complexes $H_{Zr}(-3)$ (purple), $H_{int}(+1)$ (red), $2H_{Zr}(-2)$ (light blue), and $3H_{Zr}(-1)$ (orange) are all independent of $P(O_2)$, whereas the concentration of electron (hole) increases (decreases) upon lowering $P(O_2)$, with a corresponding upshift of the Fermi level within the band gap. The $H_O(+1)$ defect, represented using a green line, shows a slope of $+1/2$. This defect involves removing a lattice oxygen and replacing it with a hydrogen. On the other hand, in the case of varying $P(H_2O)$ at a fixed $P(O_2)$, i.e., Fig. 4(b), the concentrations of H_{int}, $H_{Zr}(-3)$, $2H_{Zr}(-2)$, $3H_{Zr}(-1)$, and $4H_{Zr}(0)$ defects exhibit larger decreases upon lowering the $P(H_2O)$, while the concentration of electron and hole as well as the concentrations of V_{Zr} and V_O show weak $P(H_2O)$ dependencies. The H_O defect exhibits a slope of $-1/2$, consistent with those of the H_{int} and H_{Zr} defects as these defects all involve hydrogen being inserted into the bulk lattice.

Overall, the results presented in Fig. 4(a) demonstrate that at a fixed $P(H_2O)$, the concentration of electron (hole) exhibits a $P(O_2)^m$ dependence with $m = -1/4$ ($m = 1/4$), where m corresponds to the slope of Fig. 4. Additionally, the concentrations of the major ionic defect species V_{Zr}, V_O, H_{Zr}, and H_{int} are independent of $P(O_2)$, which is a consequence of the charge neutrality requirement accompanied by a large energetic penalty to form charged ionic defects in an ionic material with a large band gap [38]. For the scenario

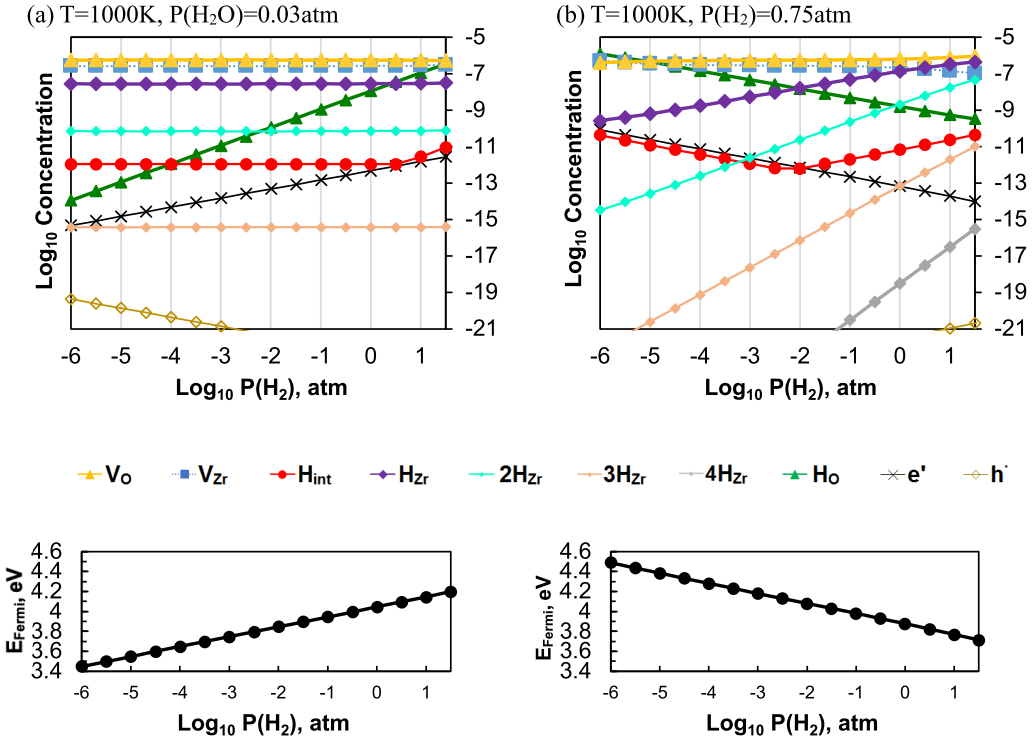

FIG. 5. (a) Concentration of the defect species per formula unit versus $P(H_2)$ obtained from the defect model for the condition of $T = 1000$ K, $P(H_2O) = 0.03$ atm. (b) The concentration of the defect species per formula unit versus $P(H_2O)$ obtained from the defect model for the condition of $T = 1000$ K, $P(H_2) = 0.75$ atm. The point defect species included in these plots are V_O (yellow triangle), V_{Zr} (blue squares), H_{int} (red circles), H_{Zr} (purple diamonds), $2H_{Zr}$ (light blue small diamonds), $3H_{Zr}$ (orange small diamonds), $4H_{Zr}$ (grey small diamonds), electron (black crosses, e'), hole (grey empty diamonds, $h^{\bullet}$), and H_O (green triangles). The corresponding Fermi levels at varying gas pressure conditions as represented in (a) and (b) are provided in (c) and (d), respectively.

of varying humidity at a fixed $P(O_2)$, see data in Fig. 4(b), the concentration of H_{Zr} and H_{int} exhibits a $P(H_2O)^m$ dependence with $m = 0.50$, and the concentration $2H_{Zr}$, $3H_{Zr}$, and $4H_{Zr}$ exhibits a $P(H_2O)^m$ dependence with $m = 1.00$, 1.50, and 2.00 respectively. The stronger $P(H_2O)$ dependence of the H_{Zr} and H_{int} concentration is in contrast to the weak $P(H_2O)$ dependence of the concentration of e', $h^{\bullet}$, V_{Zr}, and V_O [$m = -0.008$, 0.008, 0.033, and 0.017, respectively, for humidity pressures above $P(H_2O) = 10^{-5}$ atm]. These findings indicate that the amount of humidity can cause significantly larger changes in the concentration of H-related defects in bulk tetragonal ZrO_2 while only slightly altering the electronic carrier and cation/anion vacancy concentration.

C. Point defect concentration versus $P(H_2)/P(H_2O)$ at $T = 1000$ K

Figures 5(a) and 5(b) show the concentration of ionic defects and charge as a function of $P(H_2)$ at $P(H_2O) = 0.03$ atm and as function of $P(H_2O)$ at $P(H_2) = 0.75$ atm at $T = 1000$ K in tetragonal ZrO_2 as obtained from the defect model analysis. Details of the ΔG_{form}(Defect) versus E_{Fermi} plots at varying $P(H_2)$ under a fixed $P(H_2O) = 0.03$ atm and at varying $P(H_2O)$ under a fixed $P(H_2) = 0.75$ atm are provided in Fig. S6 of the SM. Upon varying the $P(H_2)$ under a fixed $P(H_2O) = 0.03$ atm, it can be seen in Fig. 5(a) that the dominant defects in bulk tetragonal ZrO_2 between $P(H_2) = 10^{-5}$–10^{1} atm are V_O and V_{Zr}, followed by $H_{Zr}(-3)$ and $H_O(+1)$ defects. The concentration of H_O becomes comparable to that of H_{Zr} when $P(H_2)$ is close to 1.0 atm, as the concentration of H_O exhibits a $P(H_2)^m$ dependence with $m = 1.0$. The concentration of electrons (holes) in tetragonal ZrO_2 under these conditions exhibits a $P(H_2)^m$ dependence with $m = 0.5$ (-0.5), and the Fermi level increases from 2.4 to 2.8 eV relative to the VBM.

When varying $P(H_2O)$ in the range of 10^{-5}–10^{1} atm under a fixed $P(H_2) = 0.75$ atm at $T = 1000$ K, it can be seen in Fig. 5(b) that the $P(H_2O)$ dependencies of electrons and holes in tetragonal ZrO_2 show opposite slopes compared to those in Fig. 5(a). This fact is due to the activity of oxygen which is proportional to $\ln[P(H_2O)/P(H_2)]$. The $P(H_2O)$ dependencies (slopes) for the concentration of electrons and holes in tetragonal ZrO_2 are -0.521 and 0.521, respectively. It is also noted that the concentration of H_{int} exhibit both positive and negative slopes in these conditions. The slope change of the H_{int} concentration versus $P(H_2O)$ profile is due to a switch of the stable H_{int} defect charge state, i.e., the self-consistent E_{Fermi} crosses the $H_{int}(+1)/H_{int}(-1)$ defect transition level upon lowering the $P(H_2O)$. For example, at $P(H_2O) = 0.25$ atm, H_{int} is in the $+1$ charge state [$H_{int}(+1)$ proton interstitial], whereas at $P(H_2O) = 0.0003$ atm, H_{int} is in the -1 charge state [$H_{int}(-1)$ hydride interstitial], as shown in Figs. S6(d) and S6(f) of the SM. Under higher $P(H_2O)$ conditions, e.g., $P(H_2O) > 3.2$ atm, the concentration of $H_{Zr}(-3)$ surpasses $V_{Zr}(-4)$ and is mainly compensated by $V_O(+2)$ to

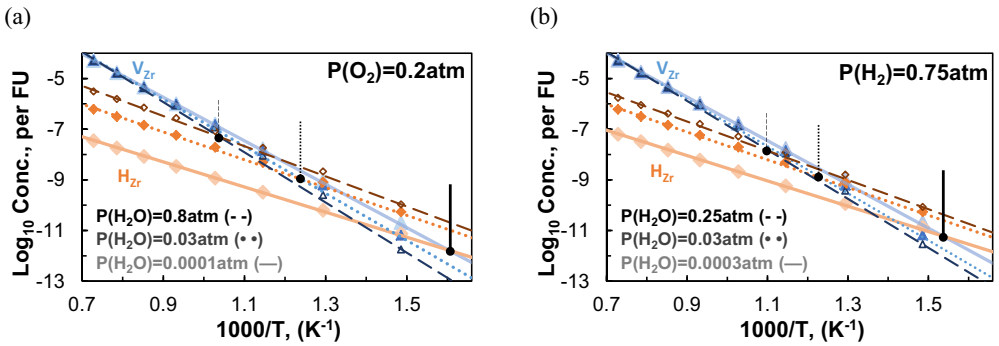

FIG. 6. The concentration of V_{Zr} (light, normal, and dark blue circles) and H_{Zr} (light, normal, and dark orange diamonds) as a function of inverse temperature ($1000/T$, K^{-1}) at various $P(H_2O)$ under (a) $P(O_2) = 0.2$ atm and (b) $P(H_2) = 0.75$ atm. The lines with different blue and orange intensities represent different $P(H_2O)$: In (a), the dashed dark-color line corresponds to $P(H_2O) = 0.8$ atm, the dotted normal-color line corresponds to $P(H_2O) = 0.03$ atm, and the solid thick light-color line corresponds to $P(H_2O) = 0.0001$ atm. In (b), the dashed dark-color line corresponds to $P(H_2O) = 0.25$ atm, the dotted normal-color line corresponds to $P(H_2O) = 0.03$ atm, and the solid dark-color thick line corresponds to $P(H_2O) = 0.0003$ atm. The crossing points of the H_{Zr} versus V_{Zr} concentration under the specified conditions are labeled with black dots and vertical lines using the same line format as each of the indicated $P(H_2O)$.

fulfill the charge neutrality requirement. On the other hand, the H_O defect with a charge state of +1, i.e., $H_O(+1)$, also becomes dominant over the $V_O(+2)$ defect in the lower $P(H_2O)$ conditions, e.g. $P(H_2O) < 10^{-5}$ atm.

D. Concentration of $V_{Zr}(-4)$ and $H_{Zr}(-3)$ in bulk tetragonal ZrO_2 versus temperature

In order to understand the effect of humidity and hydrogen defect complexes on bulk cation transport in tetragonal ZrO_2, the concentration of possible cation transport carriers, including $V_{Zr}(-4)$ and $H_{Zr}(-3)$, as a function of inverse temperature are compared, and the results are shown in Fig. 6. Additional details of the point defect concentration versus $P(H_2O)$ at fixed $P(O_2)$ or $P(H_2)$ as well as versus $P(O_2)$ or $P(H_2)$ at a fixed $P(H_2O) = 0.03$ atm at various temperatures ($T = 673$, 873, 1000, 1273, and 1473 K) are provided in Figs. S7–S10 of the SM. The corresponding intrinsic E_{Fermi} of the bulk tetragonal ZrO_2 shown in Figs. S7–S10 obtained from the defect model are provided in Fig. S11 of the SM. It is noted that in the temperature range $T = 673$–1473 K investigated in this work, the $2H_{Zr}(-2)$, $3H_{Zr}(-1)$, and $4H_{Zr}(0)$ defect complexes are less stable than the $H_{Zr}(-3)$ defect. Furthermore, as will be discussed below, their migration barriers are also greater than those of $H_{Zr}(-3)$, with a trend of increasing barriers upon increasing the number of hydrogen substitution at a Zr site due to enhanced binding of multiple trapped H's with the V_{Zr}. Hence, in this work the $H_{Zr}(-3)$ is considered as the representative hydrogen defect complex relevant for cation transport.

The model solutions of the $V_{Zr}(-4)$ and $H_{Zr}(-3)$ concentration versus T^{-1} exhibit a quasi-Arrhenius-type relation (see the van't Hoff plots in Fig. 6). The slight scattering of the data points is due to numerical instability associated with solving the coupled nonlinear equations for the concentration of the defect species and charges. For the conditions of $P(O_2) = 0.2$ atm and $P(H_2) = 0.75$ atm, it can be seen in Figs. 6(a) and 6(b) that the concentration of H_{Zr} becomes dominant relative to $V_{Zr}(-4)$ below the crossover temperature at $P(H_2O) = 0.03$ atm [$T_{cross} = 838$ K in Fig. 6(a) and $T_{cross} = 818$ K in Fig. 6(b)], and the crossover of the two defect concentrations versus T^{-1} profiles occurs at higher temperature upon increasing $P(H_2O)$: $T_{cross} = 999$ K for $P(H_2O = 0.8$ atm) in Fig. 6(a), and $T_{cross} = 910$ K for $P(H_2O) = 0.25$ atm in Fig. 6(b). This concentration crossover among the $H_{Zr}(-3)$ and $V_{Zr}(-4)$ defects indicates that the $H_{Zr}(-3)$ cation transport mechanism may become most relevant at lower temperature or higher humidity.

Despite the fact that both $V_{Zr}(-4)$ and $H_{Zr}(-3)$ concentrations versus T^{-1} profiles show similarities in both Figs. 6(a) and 6(b), i.e., the O_2-rich condition versus the H_2-rich condition, the driving forces responsible for the change in the $H_{Zr}(-3)$ concentration relative to the $V_{Zr}(-4)$ concentration are different. For the O_2-rich condition [Fig. 6(a)], the increase of the $H_{Zr}(-3)$ concentration with increasing $P(H_2O)$ is determined by the increased H activity, whereas in the H_2-rich condition, the increase of the H_{Zr} concentration is mainly driven by the increased O activity upon increasing $P(H_2O)$. As $H_{Zr}(-3)$ can be considered as a bound product of $H_{int}(+1)$ and $V_{Zr}(-4)$, the change in O activity results in analogous behavior for $H_{Zr}(-3)$ and $V_{Zr}(-4)$ versus $P(H_2O)$ under a fixed $P(H_2)$, i.e., the higher the H_2O or O activity, the easier is the formation of $H_{Zr}(-3)$ and $V_{Zr}(-4)$.

Overall, the predicted apparent formation free energy of $H_{Zr}(-3)$ as a function of inverse temperature obtained from the van't Hoff plots of Fig. 6 are in the range of 0.84–1.02 eV for the H_2 rich condition and about 0.85–1.06 eV for the O_2 condition, respectively, as summarized in Table II. A full summary of the apparent defect formation energies and defect concentration as a function of inverse temperature for all the investigated defect species is provided in Tables S3 and S4 of the SM. Compared with the 1.55–1.83-eV apparent formation free energy of $V_{Zr}(-4)$, the 0.5–1.0 eV smaller apparent formation energy of $H_{Zr}(-3)$ originates from the attractive interaction between $H_{int}(+1)$ and $V_{Zr}(-4)$ defects. While it has been suggested that frozen cation vacancies may exist in bulk tetragonal ZrO_2 when lowering the temperature, as annihilation of lattice cation vacancies may be kinetically too slow to reach thermodynamic equilibrium [3], these frozen cation vacancies can still interact with H_{int} upon

TABLE II. Summary of the apparent formation energies, ΔE_{form}, of V_{Zr} and H_{Zr} shown in Fig. 6 (i.e., slopes of the lines).

Operating conditions		Apparent formation energy of V_{Zr}	Apparent formation energy of H_{Zr}
$P(O_2) = 0.2$ atm	$P(H_2O) = 0.8$ atm	1.91 eV	1.15 eV
	$P(H_2O) = 0.03$ atm	1.78 eV	1.04 eV
	$P(H_2O) = 0.0001$ atm	1.67 eV	0.96 eV
$P(H_2) = 0.75$ atm	$P(H_2O) = 0.25$ atm	1.86 eV	1.10 eV
	$P(H_2O) = 0.03$ atm	1.78 eV	1.04 eV
	$P(H_2O) = 0.0003$ atm	1.67 eV	0.96 eV

increasing humidity or lowering operating temperature, due to the fact that the diffusion rate of H_{int} is orders of magnitude higher than the cation transport kinetics [11]. In other words, the fundamental defect interactions between the cation vacancies and the H_{int} defects and the much faster H_{int} transport rate may result in formation of $H_{\text{Zr}}(-3)$ that replaces $V_{\text{Zr}}(-4)$ in the material even for a metastable phase with excess cation vacancies, and therefore the cation diffusion kinetics can still switch from the $V_{\text{Zr}}(-4)$ mechanism to the $H_{\text{Zr}}(-3)$ mechanism upon increasing humidity or lowering temperature in the material with kinetically frozen-in cation vacancies. Further discussions on the coupling of H_{int} defect and transport with cation diffusion will be detailed below in Sec. IV.

IV. MODELING OF BULK CATION TRANSPORT

A. Cation migration mechanisms

The energetics of the cation diffusion for the Zr^{4+} and Y^{3+} migration involving isolated and bound Schottky defect complexes in bulk tetragonal ZrO_2 was recently investigated based on density functional theory (DFT) simulations [15]. The results indicate a synergetic effect associated with the defect interactions between the cation vacancy and anion vacancies and reduction of the migration barriers for the partially and fully bound Schottky defect clusters. In addition, due to the tetragonal crystal symmetry, it was also identified that the out-of-*ab*-plane [i.e., out of the (001) plane] cation migration exhibits lower migration barriers than the in-plane hopping, indicating anisotropic cation transport in the tetragonal ZrO_2 [15]. The migration barriers of a Ce hop in cubic CeO_2 with a single Ce vacancy, a partially bound Schottky defect, and a fully bound Schottky defect were also investigated by Beschnitt *et al.* [39] with the empirical pair potentials and the DFT modeling using the GGA + U method. The calculated GGA + U migration barriers are in the range of 3.98–4.94 eV, about 0.54–2.72 eV higher than the Zr migration barriers reported in the previous study for the tetragonal ZrO_2 [15].

Figure 7 shows the calculated energy profiles and the initial and transition state configurations for the out-of-*ab*-plane lattice Zr migration via the $H_{\text{Zr}}(-3)$ transport carrier (the configurations were created using the VESTA program [40]). Similarly, Fig. 8 shows the same set of results for the in-*ab*-plane lattice Zr migration via the $H_{\text{Zr}}(-3)$ transport. It is noted that Figs. 7 and 8 only contain half of the $H_{\text{Zr}}(-3)$ transport mechanism, i.e., $H_{\text{Zr}}(-3) \rightarrow V_{\text{Zr}}(-4) + H_{\text{int}}(+1)$, and completion of the $H_{\text{Zr}}(-3)$ hop requires restoring the $H_{\text{Zr}}(-3)$ state by moving the $H_{\text{int}}(+1)$ into the migrated $V_{\text{Zr}}(-4)$, i.e., $V_{\text{Zr}}(-4) + H_{\text{int}}(+1) \rightarrow H_{\text{Zr}}(-3)$, as will be shown later in Fig. 10(a). Since the barriers of $H_{\text{int}}(+1)$ migration into $V_{\text{Zr}}(-4)$ are much smaller than the barriers of the cation hop shown in Figs. 7 and 8, here it is mainly focused on the energy profiles and the migration barriers for the first half part of the $H_{\text{Zr}}(-3)$ transport mechanism. The energy profiles and configurations for the out-of-*ab*-plane $V_{\text{Zr}}(-4)$ hop and in-*ab*-plane $V_{\text{Zr}}(-4)$ hop are provided in Figs. S12 and S13 of the SM, respectively. The calculated barriers of the $H_{\text{Zr}}(-3)$ and $V_{\text{Zr}}(-4)$ migrations are summarized in Table III. The stable charge state of H_{Zr} within the range of conditions considered in this study is -3, as shown in Fig. 3 and in Figs. S5 and S6 of the SM. The migration barriers of H_{Zr} in the other defect charge states (-1 and -2) were also calculated but no significant change in the migration barriers (Fig. S14 of the SM) was identified. Therefore, since the $H_{\text{Zr}}(-3)$ is the most stable H_{Zr} charge state spanning a range of ~3 eV within the band gap based on the *ab initio* charged defect analysis (the slope of H_{Zr} versus E_{Fermi} equal to -3 and the predicted intrinsic E_{Fermi} is 1–2 eV above the H_{Zr} transition level) the possibility of H_{Zr} migration in other defect charge states was ruled out. As a result, the other charge states of H_{Zr} are thermodynamically unfavorable for being cation transport carriers with comparable migration barriers to $H_{\text{Zr}}(-3)$. Furthermore, the energy profiles of $2H_{\text{Zr}}(-2)$ and $4H_{\text{Zr}}(0)$ migrations were also investigated (the results not shown), and for each of the defect transport mechanism the sum of the migration barrier and of the formation free energy was found to be higher than those of the $H_{\text{Zr}}(-3)$. Particularly, the formation free energies of $2H_{\text{Zr}}(-2)$, $3H_{\text{Zr}}(-1)$, and $4H_{\text{Zr}}(0)$ have been shown to be higher than that of H_{Zr} above $T = 673$ K (see, e.g., Fig. 3 and Figs. S5 and S6 of the SM). Combining these findings with the results that the $2H_{\text{Zr}}(-2)$, $3H_{\text{Zr}}(-1)$, and $4H_{\text{Zr}}(0)$ defects are less stable than $H_{\text{Zr}}(-3)$ in the conditions specified in this work, it can be concluded that cation transport via the $2H_{\text{Zr}}(-2)$, $3H_{\text{Zr}}(-1)$, and $4H_{\text{Zr}}(0)$ carriers is less relevant and can be excluded from further analysis.

It should be noted that the energy profiles for the cation migration via the $H_{\text{Zr}}(-3)$ and $\mathbf{n}H_{\text{Zr}}$ carriers are asymmetric, due to the presence of the incoporated H species that breaks the symmetry of the initial state versus the final state. This is in contrast to the symmetric energy profile of the $V_{\text{Zr}}(-4)$ hop [15]. In addition, in the case of $H_{\text{Zr}}(-3)$ transport, a total of 12 cNEB calculations involving H and Zr co-migration, including four in-*ab*-plane hops and eight out-of-*ab*-plane hops, were also performed, and none of the calculated migration barriers were found to be lower than

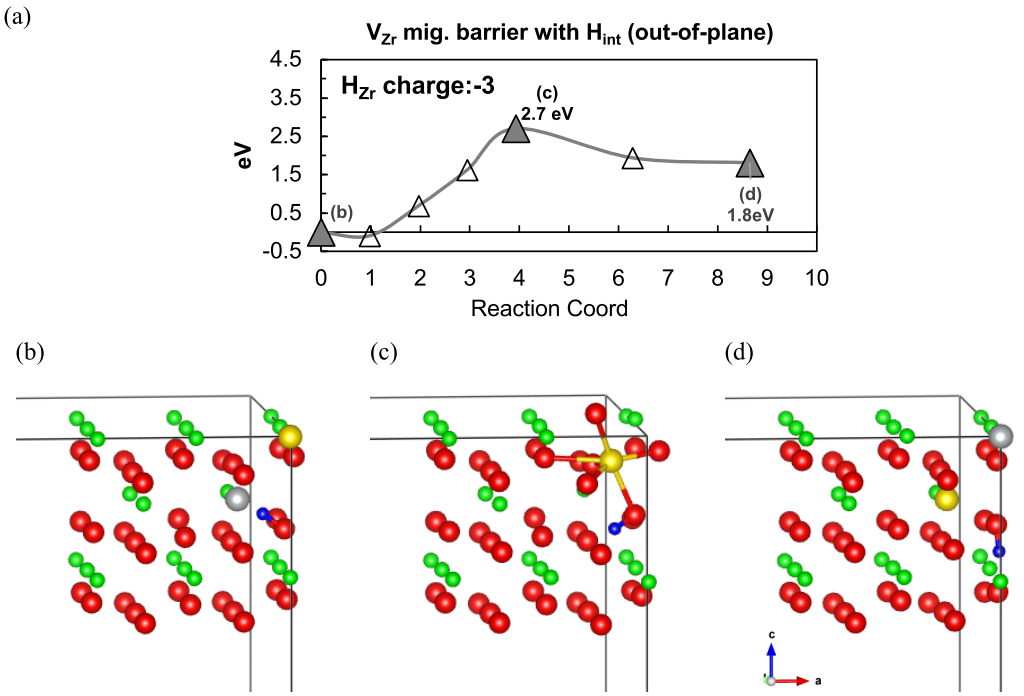

FIG. 7. (a) The representative energy profile of the out-of-*ab*-plane $H_{Zr}(-3)$ migration, where the value of -3 in parentheses indicates the charge state of the defect. Panels (b)–(d) show the atomic configurations of the initial, saddle-point, and transition state images indicated with filled triangle symbols in (a). The red, green, blue, and grey spheres represent lattice O, lattice Zr, and incorporated H. The migrating Zr and H_{Zr} (or V_{Zr} after the migrating Zr hops into H_{Zr}) are shown in yellow and grey spheres, respectively. The images were created using the VESTA program (same below) [40]. Note that the energy profile shown in (a) only contains half of the $H_{Zr}(-3)$ migration mechanism, i.e., $H_{Zr}(-3) \rightarrow V_{Zr}(-4) + H_{int}(+1)$, and completion of the $H_{Zr}(-3)$ hop requires restoring the $H_{Zr}(-3)$ state by moving the $H_{int}(+1)$ into the migrated $V_{Zr}(-4)$.

the barrier of the sequential Zr and H migration shown in Fig. 7 for the out-of-*ab*-plane H_{Zr} migration (or Fig. 8 for the in-*ab*-plane H_{Zr} migration). This is due to the fact that the transition state image of the cation migration is mainly controlled by the local compressive Zr-O environments [14], and the presence of a nearby H does not release the stress imposed by the Zr-O compressive environment of the saddle-point images.

As shown in Figs. 7and 8, the final states of the H_{Zr} migration, i.e., a dissociated $H_{int}(+1)$ and $V_{Zr}(-4)$ pair, are 1.8 and 1.5 eV higher than their corresponding initial H_{Zr} states, indicating that an attractive interaction between $H_{int}(+1)$ and $V_{Zr}(-4)$ is at least 1.5 eV when the energy of the initial H_{Zr} state is referenced with respect to that of the final state. Note that this value can be further increased if the $H_{int}(+1)$ and $V_{Zr}(-4)$ defects are farther apart. The +1.5–1.8-eV energy difference between the initial state and the final state of the $H_{Zr}(-3)$ migration shown in Figs. 7 and 8 suggests that the probability of finding a dissociated $H_{int}(+1)$ and $V_{Zr}(-4)$ pair is lower than their bound product, $H_{Zr}(-3)$. The reverse barrier for hopping from the dissociated $H_{int}(+1)$ and V_{Zr} (-4) to $H_{Zr}(-3)$ states is lower than the barrier for the forward migration.

In the following Sec. IV B, we focus on modeling the bulk cation diffusivities with and without H species present, for the case of $H_{Zr}(-3)$ and Zr^{4+} species, respectively. For the $H_{Zr}(-3)$ transport, the scenario of dissociating $H_{Zr}(-3)$ to form $V_{Zr}(-4)$ and $H_{int}(+1)$, i.e., the forward reaction of Figs. 7 and 8, is considered as the rate-limiting step of the $H_{Zr}(-3)$ migration at the defect themodynamic equilibria.

B. Bulk cation diffusivities

In order to assess the trends of cation diffusion between the two $V_{Zr}(-4)$ and $H_{Zr}(-3)$ mechanisms, a simple three-dimensional random-walk model is adopted [39,41], with a pre-exponential D_0 term (containing the attempt frequency, hopping distance, geometry factor, correlation factor, etc.) fixed to a value of 1.296×10^{-3} cm^2/s for the two $V_{Zr}(-4)$ and $H_{Zr}(-3)$ pathways. The pre-exponential D_0 term mainly contributes to the absolute D values, i.e., a constant shift of D, while the T dependence, which is one of the main focuses of this study, is less influenced upon varying D_0. Therefore, a simple analysis is performed by examining the variation in the slopes of the dependence on $P(H_2O)$ for the two cation diffusion mechanisms, i.e., $\log_{10}[D_{Zr}(V_{Zr})]$ and $\log_{10}[D_{Zr}(H_{Zr})]$ versus T^{-1}. The results are shown in Fig. 9, where the calculated bulk cation diffusivities along the out-of-*ab*-plane and in-*ab*-plane pathways, at $P(O_2) = 0.2$ atm and $P(H_2) = 0.75$ atm, are included. It is noted that the calculated bulk $D_{Zr}(H_{Zr})$ is based on the scenario of the forward reactions represented in Figs. 7 and 8. To illustrate the effect of humidity, cation diffusivities at varying $P(H_2O)$ values are represented using different line types and color intensities. The extracted activation energies in the Arrhenius-type plots of Fig. 9 are summarized in Table IV.

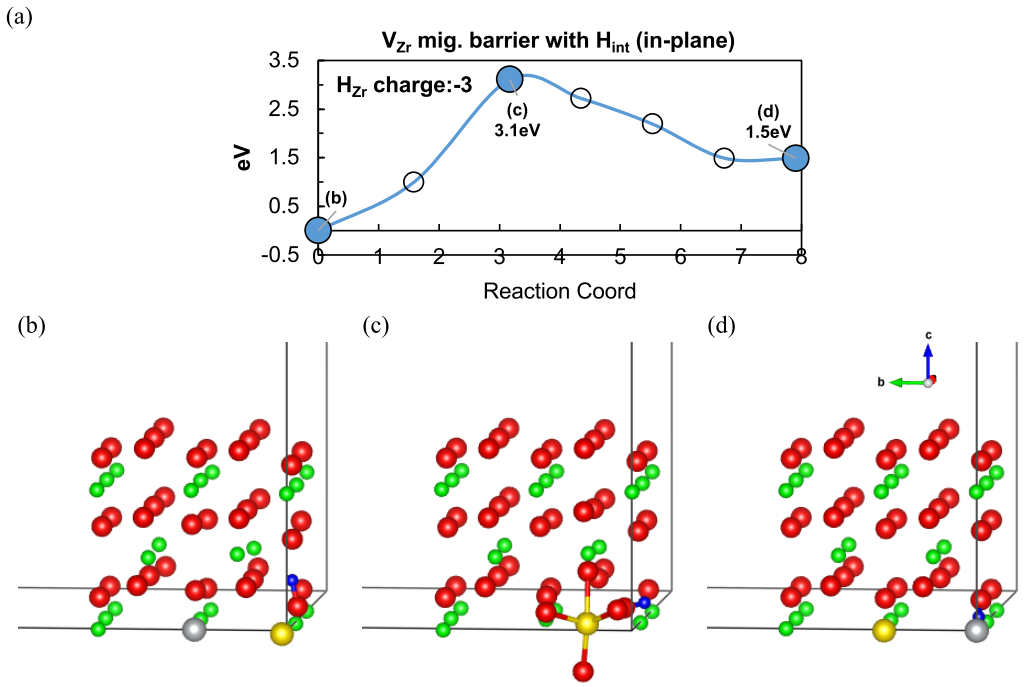

FIG. 8. (a) The representative energy profile of the in-*ab*-plane $H_{Zr}(-3)$ migration. Panels (b)–(d) are the corresponding initial-state, saddle-point configuration, and transition state images, indicated with filled circle symbols in (a). The red, green, and blue spheres represent lattice O, lattice Zr, and incoporated H. The migrating Zr and V_{Zr} after the migrating Zr hops into $H_{Zr}(-3)$ are shown in yellow and grey spheres, respectively. Note that the energy profile shown in (a) only contains half of the $H_{Zr}(-3)$ migration mechanism, i.e., $H_{Zr}(-3) \rightarrow V_{Zr}(-4) + H_{int}(+1)$, and completion of the $H_{Zr}(-3)$ hop requires restoring the $H_{Zr}(-3)$ state by moving the $H_{int}(+1)$ into the migrated $V_{Zr}(-4)$.

It can be seen in Fig. 9 that a crossover of the out-of-*ab*-plane cation diffusivities, $D_{Zr}(H_{Zr})$ and $D_{Zr}(V_{Zr})$ takes place similar to the concentration crossover observed for the H_{Zr} and V_{Zr} species. The diffusivities crossover in Fig. 9(c) takes place at $P(O_2) = 0.2$ atm and in Fig. 9(d) for the $P(H_2) = 0.75$ atm condition. Additionally, it can be observed that $D_{Zr}(H_{Zr})$ is greater than the $D_{Zr}(V_{Zr})$ below the crossover temperature ($T_{cross} = 700$ K at $P(H_2O) = 0.03$ atm; $T_{cross} = 843$ K at $P(H_2O) = 0.8$ atm and $T_{cross} = 787$ K at $P(H_2O) = 0.25$ atm). On the other hand, for the in-*ab*-plane $D_{Zr}(H_{Zr})$ and $D_{Zr}(V_{Zr})$ shown in Figs. 9(a) and 9(b), the crossover occurs at a much lower temperature ($T = 480$–592 K), which is outside the temperature range of the plots. This crossover between the $D_{Zr}(H_{Zr})$ and $D_{Zr}(V_{Zr})$ at lower temperature is mainly controlled by the apparent formation energy difference between the two transport carriers, i.e., the difference in the apparent formation energies between the H_{Zr} versus V_{Zr} defects. This difference is about 0.4–0.7 eV (see Table II), which is larger than the difference of 0.1–0.3 eV in the corresponding migration barriers (see Table III). Similarly, upon increasing $P(H_2O)$, the crossover between $D_{Zr}(H_{Zr})$ and $D_{Zr}(V_{Zr})$ is shifted toward the left-hand side of the plot, i.e., to higher temperature. The results indicate that increasing the humidity content will enhance the $D_{Zr}(H_{Zr})$ diffusivity, and consequently the cation diffusion mechanism will become dominant over the $D_{Zr}(V_{Zr})$ diffusivity below the crossover temperature. By comparing the calculated cation diffusivities under the conditions of $P(O_2) = 0.2$ atm and $P(H_2) = 0.75$ atm, it can be seen in Figs. 9(a) and 9(b) [or Fig. 9(c) versus Fig. 9(d) for the in-*ab*-plane diffusion] that the overall cation diffusivities in these two conditions are very similar.

TABLE III. Summary of the migration barriers of $H_{Zr}(-3)$ and $V_{Zr}(-4)$ for the out-of-*ab*-plane hop and the in-*ab*-plane hop in the forward direction. The energy profiles and configurations for the out-of-*ab*-plane $V_{Zr}(-4)$ hop and the in-plane $V_{Zr}(-4)$ hop are provided in Figs. S12 and S13 of the SM, respectively.

	Migration barrier of $H_{Zr}(-3)$	Migration barrier of $V_{Zr}(-4)$
Out-of-*ab*-plane hop	2.7 eV	2.4 eV
In-*ab*-plane hop	3.1 eV	3.0 eV

Due to anisotropy of the tetragonal ZrO_2 [15], the migration barriers of the in-*ab*-plane $H_{Zr}(-3)$ [and $V_{Zr}(-4)$] hop are higher than those of the out-of-*ab*-plane hop, as summarized in Table III. These differences in barrier heights result from lower in-*ab*-plane diffusion versus the out-of-*ab*-plane diffusion for both the $D_{Zr}(H_{Zr})$ and $D_{Zr}(V_{Zr})$, i.e., Fig. 9(c) versus Fig. 9(a) at $P(O_2) = 0.2$ atm [or Fig. 9(d) versus Fig. 9(b) at $P(H_2) = 0.75$ atm]. The migration barrier of the H_{Zr} out-of-*ab*-plane hop is found to be 0.3 eV higher than the barrier of the $V_{Zr}(-4)$ out-of-*ab*-plane hop, whereas the H_{Zr} in-plane hop exhibits a migration barrier that is 0.1 eV higher than the $V_{Zr}(-4)$ for in-*ab*-plane hop. Consequently, the smaller barrier increase between the $H_{Zr}(-3)$ and $V_{Zr}(-4)$ migration leads to a crossover temperature for the in-*ab*-plane

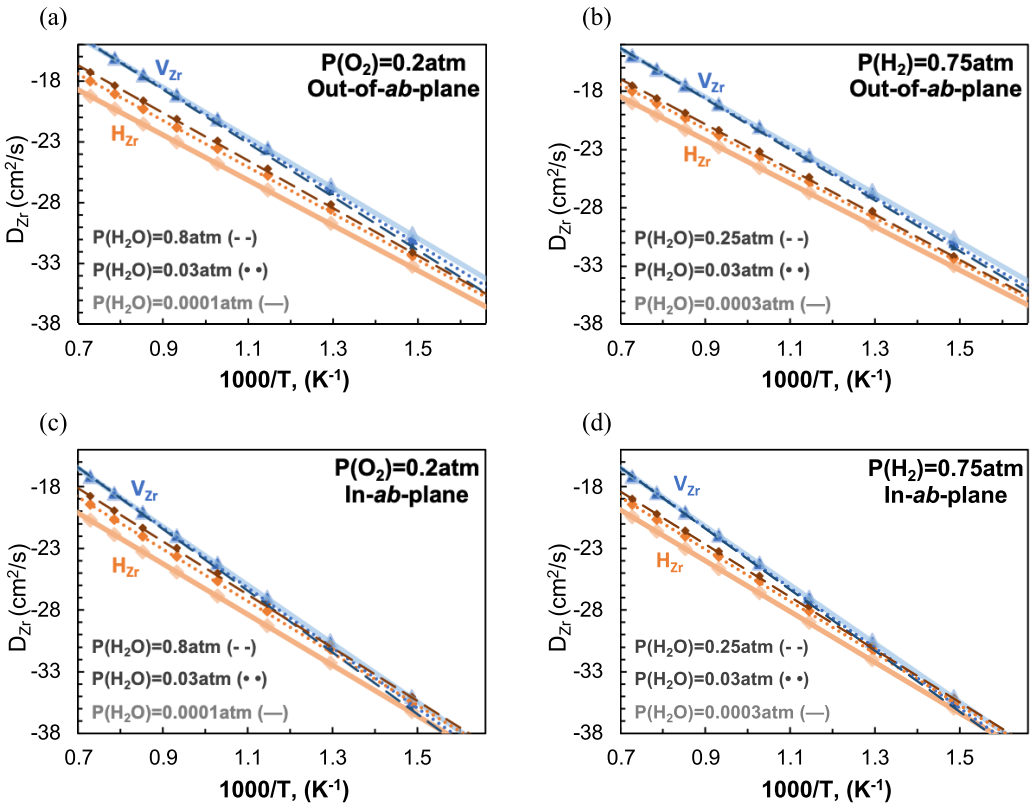

FIG. 9. The model predicted $D_{Zr}(V_{Zr})$, in blue color, and $D_{Zr}(H_{Zr})$, in orange color versus $1000/T$ (K^{-1}) for (a) out-of-*ab*-plane diffusion at $P(O_2) = 0.2$ atm, (b) out-of-*ab*-plane diffusion at $P(H_2) = 0.75$ atm, (c) in-*ab*-plane diffusion at $P(O_2) = 0.2$ atm, and (d) in-*ab*-plane diffusion at $P(H_2) = 0.75$ atm. Three $P(H_2O)$ conditions are represented with different color intensities and different types of lines [dashed, dotted, and solid lines for $P(H_2O)$ from high to low]. The crossing points of the H_{Zr} versus V_{Zr} concentration under the specified conditions are indicated with black dots and vertical lines.

diffusion that is higher than the out-of-*ab*-plane diffusion for the $D_{Zr}(H_{Zr})$ and $D_{Zr}(V_{Zr})$.

Overall, the calculated diffusion coefficients in this work reveal that bulk cation diffusion will transit from the V_{Zr} mechanism at high temperatures to the H_{Zr} pathway below 300–500 °C under $P(H_2O) = 0.03$–0.8 atm, and the major driving force of such transition comes from the apparent formation free energy of H_{Zr} which is lowered by 0.5–0.7 eV more than that of V_{Zr} (Fig. 4). This effect takes place due to the attractive interaction between $H_{int}(+1)$ and $V_{Zr}(-4)$ under sufficient humidity at lower temperature. A second but minor contribution to the apparent activation barrier difference between the $D_{Zr}(H_{Zr})$ and $D_{Zr}(V_{Zr})$ comes from the migration barrier variation of the $H_{Zr}(-3)$ versus $V_{Zr}(-4)$ (+0.3 eV for the out-of-*ab*-plane migration and +0.1 eV for the in-*ab*-plane migration). Therefore, the *ab initio* thermodynamic analysis described above was able to identify the operating conditions under which humidity can trigger the H_{Zr} transport in the

TABLE IV. Summary of the apparent activation energies ΔE_a, of $D_{Zr}(H_{Zr})$ and $D_{Zr}(V_{Zr})$ shown in Figure 9.

Diffusion pathway and gas condition		$P(H_2O)$	ΔE_a of $D_{Zr}(H_{Zr})$)	ΔE_a of $D_{Zr}(V_{Zr})$
Out-of-*ab*-plane hop	$P(O_2) = 0.2$ atm	0.8 atm	3.80 eV	4.31 eV
	[Fig. 9(a)]	0.03 atm	3.69 eV	4.16 eV
		0.0001 atm	3.66 eV	4.07 eV
	$P(H_2) = 0.75$ atm	0.25 atm	3.75 eV	4.24 eV
	[Fig. 9(b)]	0.03 atm	3.69 eV	4.15 eV
		0.0003 atm	3.66 eV	4.07 eV
In-*ab*-plane hop	$P(O_2) = 0.2$ atm	0.8 atm	4.20 eV	4.91 eV
	[Fig. 9(c)]	0.03 atm	4.09 eV	4.76 eV
		0.0001 atm	4.06 eV	4.67 eV
	$P(H_2) = 0.75$ atm	0.25 atm	4.15 eV	4.84 eV
	[Fig. 9(d)]	0.03 atm	4.09 eV	4.75 eV
		0.0003 atm	4.06 eV	4.67 eV

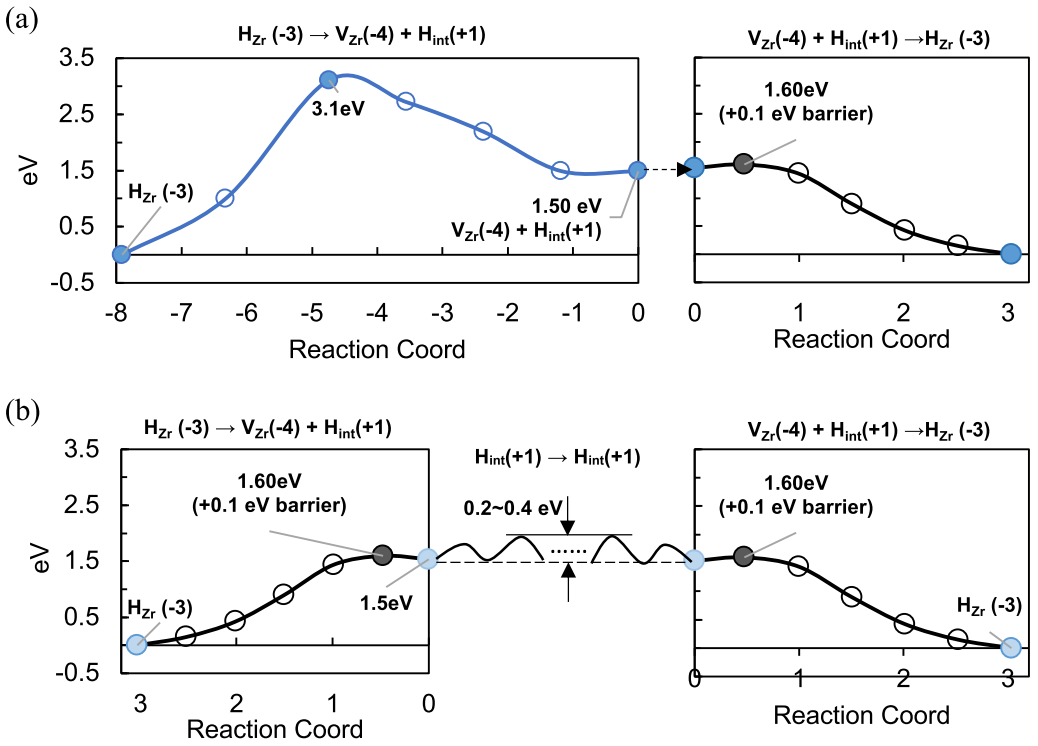

FIG. 10. (a) The energy profile of a full $H_{Zr}(-3)$ migration. The left-hand side figure is the same as Fig. 8 with a shift of the reaction coordinate to set the final state [dissociated $H_{int}(+1)$ and $V_{Zr}(-4)$ defect pair] of Fig. 8 to a value of 0 in Fig. 10. The energy profile of the subsequent $H_{int}(+1)$ migration is shown on the right-hand side figure, with a barrier of +0.1 eV relative to the state of the dissociated $H_{int}(+1)$ and $V_{Zr}(-4)$ defect pair [+1.60 eV relative to the initial or final $H_{Zr}(-3)$ state]. The atomistic configurations indicated in this energy profile are provided in Fig. S13 of the SM. (b) Combined schematics of the energy profile of $H_{int}(+1)$ migrating away from the V_{Zr}. The drawing in the middle of the figure is taken from the calculated results shown in Figs. S13 and S14 of the SM.

temperature range 300–700 °C and as function of crystallographic orientation.

C. Coupling of cation diffusion with *H* transport

As previously shown in Figs. 7 and 8, the $H_{Zr}(-3)$ migration involves dissociation of the $H_{Zr}(-3)$ defect to form separate $V_{Zr}(-4)$ and $H_{int}(+1)$ defects (see the final-state configurations of Figs. 7 and 8). For completion of the $H_{Zr}(-3)$ hop, which restores the original $H_{Zr}(-3)$ state on a nearest-neighbor Zr lattice, a subsequent $H_{int}(+1)$ hop into the $V_{Zr}(-4)$ will be needed. The corresponding migration barrier calculated in this work has a value of 0.10 eV relative to the total energy of the dissociated $V_{Zr}(-4)$ and $H_{int}(+1)$ species (+1.60 eV relative to the initial $H_{Zr}(-3)$ state), as shown in Fig. 10. The asymmetric energy profile revealed in Fig. 10 indicates that for a complete $H_{Zr}(-3)$ hop, the $H_{Zr}(-3)$ migration can occur in two different sequential steps, a swap of a lattice Zr with the $H_{Zr}(-3)$ followed by the hopping of the dissociated $H_{int}(+1)$ back to the $V_{Zr}(+4)$, i.e., the forward reaction of Fig. 10, or the hydrogen escaping from the $H_{Zr}(-3)$ to form a $H_{int}(+1)$ and a $V_{Zr}(+4)$ followed by a subsequent $V_{Zr}(+4)$ migration to bind with the escaped $H_{int}(+1)$, i.e., the backward reaction of Fig. 10. In both cases, the largest diffusion barrier is seen for the cation movement, hence the rate of cation diffusion via the $H_{Zr}(-3)$ carrier is controlled by the barriers shown in Figs. 7 and 8.

In addition to the cation diffusion, the rates of hydrogen transport via the $H_{Zr}(-3)$ carrier can also be calculated based on the migration barrier shown in Fig. 10 and compared with $H_{int}(+1)$ diffusion. This is motivated by the fact that the $H_{Zr}(-3)$ defect also contains a hydrogen. The right-hand-side plot of Fig. 10 indicates a +1.6 eV barrier [relative to the $H_{Zr}(-3)$ state for the H to escape from the $H_{Zr}(-3)$. The subsequent *H* migration away from the original H_{Zr} site was found to have a barrier of +0.4 eV (see Fig. S15 of the SM), which gives an overall barrier of 1.9 eV for the *H* diffusion via the $H_{Zr}(-3)$ carrier, i.e., for a *H* escaping from a $H_{Zr}(-3)$ and migrating to bind with another $V_{Zr}(-4)$. In contrast, although the equilibrium $H_{int}(+1)$ concentration was predicted to be 4–6 orders of magnitude lower than $H_{Zr}(-3)$ (see Table S3 of the SM), the migration barriers of an isolated $H_{int}(+1)$ hop are calculated to be about 0.2–0.4 eV (see Fig. S16 of the SM). These simulated hydrogen migration barriers can be combined with the calculated $H_{Zr}(-3)$ and $H_{int}(+1)$ defect concentration from the defect model (Table S3 of the SM) to evaluate the hydrogen diffusivities. The corresponding results will be discussed in the following section.

D. Calculated cation and hydrogen diffusivities and comparison with experiments

In Fig. 11, the modeled bulk cation and hydrogen diffusivities based on cation vacancy migration [$D_{Zr}(V_{Zr})$] and

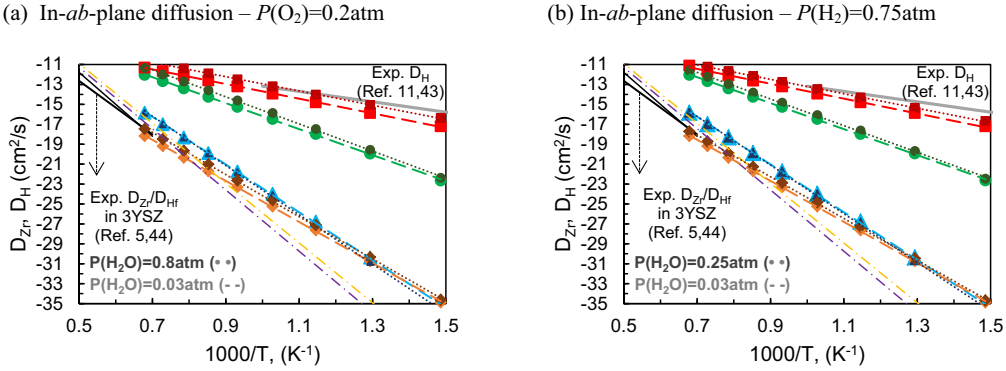

FIG. 11. The predicted $D_H(H_{int})$, in red color, and $D_H(H_{Zr})$, in orange color, $D_{Zr}(V_{Zr}\text{-}V_O)$ with a purple dash-dotted line, and $D_{Zr}(V_O\text{-}V_{Zr}\text{-}V_O)$, with a yellow dash-dotted line in the bulk tetragonal ZrO_2. The modeled $D_{Zr}(V_{Zr}\text{-}V_O)$ and $D_{Zr}(V_O\text{-}V_{Zr}\text{-}V_O)$ are provided in Fig. S17 of the SM. For comparison, the in-*ab*-plane cation diffusivities of $D_{Zr}(H_{Zr})$ and $D_{Zr}(V_{Zr})$ [same as those of Figs. 9(c) and 9(d)] are also indicated. (a) $P(O_2) = 0.2$ atm, and (b) $P(H_2) = 0.75$ atm. Two $P(H_2O)$ conditions are represented with different color intensities and different types of lines [dashed and dotted for $P(H_2O)$ from high to low]. A pre-exponential factor of 1.296×10^{-2} cm^2/s is used for the modeled $D_H(H_{int})$ and $D_H(H_{Zr})$. The reported experimental hydrogen diffusivity (Exp. D_H, represented using a grey solid line) from Refs. [11,43] and the experimental Zr diffusivity (Exp. D_{Zr}, represented using a black solid line) from Refs. [5,44] are also provided in the plots. The apparent activation energies of $D_H(H_{int})$ and $D_H(H_{Zr})$ are about 1.4–1.5 eV and 2.6 eV, respectively, whereas the apparent activation energies of $D_{Zr}(V_{Zr}\text{-}V_O)$ and $D_{Zr}(V_O\text{-}V_{Zr}\text{-}V_O)$ are about 6 eV.

hydrogen interstitial migration [$D_H(H_{int})$], as well as the cation and hydrogen migration involving the $H_{Zr}(-3)$ defect [i.e., $D_{Zr}(H_{Zr})$ and $D_H(H_{Zr})$], are summarized. Here, the lower $H_{int}(+1)$ migration barrier of 0.2 eV is used in the calculated $D_H(H_{int})$ [42]. The experimental cation and hydrogen diffusivities reported in the literature are also included in Fig. 11 for comparison [11,43]. It can be seen in Fig. 11, that the calculated hydrogen diffusivity via the $H_{Zr}(-3)$ carrier, $D_H(H_{Zr})$, is much lower than that of the H_{int} transport [$D_H(H_{int})$]. Therefore, the results obtained in this study predict that the most stable hydrogen defect species in the bulk tetragonal ZrO_2 is the $H_{Zr}(-3)$ defect, whereas the most active hydrogen transport is associated with the $H_{int}(+1)$ migration, since the barrier for H to escape from the $H_{Zr}(-3)$ defect is 1.2–1.4 eV higher than the $H_{int}(+1)$ migration. In other words, the $V_{Zr}(-4)$ defect mainly acts as a trapping site for the $H_{int}(+1)$, which can slow down the rate of hydrogen transport in the bulk tetragonal ZrO_2. Comparing the modeled hydrogen diffusivities with the reported experimental hydrogen diffusivities (D_H) [11,43] (grey line in Fig. 11), the results also indicate that the diffusivities of the hydrogen interstitial (H_{int}) mechanism provide better agreement with the experimental measurements.

Since no experimental cation diffusivities can be found in the literature for the undoped tetragonal ZrO_2, the experimental Zr diffusivities in the 3-mol % yttria stabilized tetragonal ZrO_2 from Ref. [44] are included in Fig. 11. Furthermore, assessments on the cation diffusivities via the cation vacancy-oxygen vacancy defect cluster mechanisms (i.e., fully-bound V_O-V_{Zr}-V_O partially bound V_{Zr}-V_O Schottky defect cluster) were also performed by taking into account the defect interaction energy and the migration barriers reported in Ref. [15] into the defect model and the diffusion formalism. The results are further described in Fig. S17 of the SM, where the calculated Zr diffusivities via the fully bound V_O-V_{Zr}-V_O carrier and via the partially bound V_{Zr}-V_O carrier are 0.5–6 orders of magnitude lower than the $D_{Zr}(V_{Zr})$, depending on temperature (between $T = 673$ K and $T = 1473$ K). Also, as $D_{Zr}(V_{Zr}\text{-}V_O)$ and $D_{Zr}(V_O\text{-}V_{Zr}\text{-}V_O)$ exhibit greater diffusivities at higher T ($T > 1573$ K), surpassing $D_{Zr}(V_{Zr})$, the fully bound or partially bound carriers can become the faster cation transport mechanisms. The predicted apparent activation energies of $D_{Zr}(V_{Zr})$ are within 3.66–4.91 eV (see Table IV), whereas the experimental activation energies range from 5.3 to 6.2 eV for the experimental Zr diffusivities (D_{Zr}) of 3-mol % yttria stabilized tetragonal ZrO_2 [5,44]. The modeled $D_{Zr}(V_{Zr}\text{-}V_O)$ and $D_{Zr}(V_O\text{-}V_{Zr}\text{-}V_O)$ and their apparent activation energies (about 6.0 eV) are in better agreement than the $D_{Zr}(V_{Zr})$ mechanism with the experimental values which are measured at temperatures greater than the modeled temperature range ($T = -1473$ K) [5,44]. Leaving aside the difference in the yttria substitution concentration between the experimental measurements and the modeling results, both the single V_{Zr} and bound Schottky defect related cation diffusivities are predicted to have close values in the temperature range of 1473–2000 K, making a definite mechanistic assignment difficult only based on their values within a small range of temperatures as well as when considering the spread of the experimentally determined cation diffusivities (about two orders of magnitude for the spread of the experimental data in the temperature range of $T = 1373$–1973 K) [44]. Nonetheless, the transition between these two cation transport mechanisms is predicted in the modeling results: at sufficiently high temperature, the cation transport via the Schottky defect clusters mechanisms will become activated. As formation of the Schottky defect clusters contains formation of both the cation vacancies and anion vacancies, the apparent entropy, i.e., the extrapolated intercept at $T = \infty$ in the van't Hoff plots, of the Schottky defect cluster formation is found to be greater than that of the isolated cation vacancy formation due to the additional contribution from the vibrational free energy associated with anion vacancy formation to form gas phase O_2 or H_2O at high

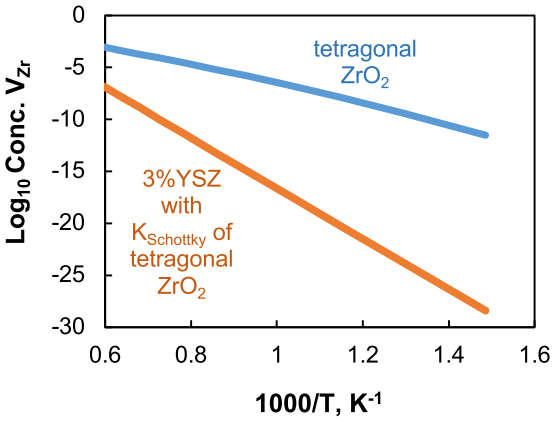

FIG. 12. Variation of the V_{Zr} concentration versus inverse of temperature for the undoped tetragonal ZrO_2 as obtained from the defect model (the blue line), and for the 3-mol % YSZ with the assumption of the same Schottky defect formation equilibrium constant ($K_{Schottky}$) as the undoped ZrO_2 (the orange line). The apparent formation energies of V_{Zr} taken from the slopes of the lines in the plot are 1.8 eV (blue line) and 4.8 eV (orange line), respectively.

temperature. In other words, the single cation vacancy formation reaction, defined as $Zr_x + O_2 \rightarrow V_{Zr}(q) + ZrO_2 - qh^\bullet$ [where q is the charge state of V_{Zr} and $h^\bullet$ is the hole as defined in Table I; for example, the formation of $V_{Zr}(-4)$ can be expressed as $Zr_x + O_2 \rightarrow V_{Zr}(-4) + ZrO_2 - (-4)h^\bullet$], also involves the O_2 gas phase (or H_2O-H_2) on the reactant side, which destabilizes the reaction with increasing temperature, whereas the O_2 (or H_2O-H_2) gas effect was further balanced by the anion vacancy formation in the Schottky defect formation. Hence, the modeling results indicate that another transition in the bulk cation transport mechanisms, V_{Zr} versus the fully or partially bound Schottky defects can also occur for the tetragonal ZrO_2 at higher temperature, in addition to the low temperature transition between V_{Zr} and H_{Zr}, as shown in Fig. 11.

Despite the agreement found for the predicted Zr diffusivities and for the predicted apparent activation energies, it should also be emphasized that the 3-mol % yttria substitution can have a substantial amount of oxygen vacancies in the bulk tetragonal ZrO_2, i.e., the introduced yttria substitution is compensated by oxygen vacancies with a concentration equal to half of the Y content as required in order to maintain charge neutrality. A further analysis was performed in this study by assuming that the equilibrium constant of the Schottky defect formation ($K_{Schottky}$) is independent of the yttria substitution content [45], and the results are shown in Fig. 12. By using an equilibrium constant $K_{Schottky}$ obtained from the tetragonal-ZrO_2 defect thermodynamic model, i.e., $K_{Schottky} = [V_{Zr}][V_O]^2$, for the 3-mol % YSZ, the results suggest that the higher Vo concentration in 3-mol % YSZ than in the tetragonal ZrO_2 will decrease the V_{Zr} concentration for the cation transport [Fig. 12(a)]. In addition, a larger slope can be seen in Fig. 12(a) for the V_{Zr} concentration versus $1/T$ of the 3-mol % YSZ, indicating a formation energy of V_{Zr} greater than that of the undoped tetragonal ZrO_2. The apparent formation energies of V_{Zr} taken from the slopes of the lines in the plot are 1.8 and 4.8 eV for the tetragonal ZrO_2 and for the 3-mol % YSZ, respectively. The 3-eV difference in the derived apparent formation energies between the tetragonal ZrO_2 and the 3-mol % YSZ can also be simply realized by that the formation free energy of V_{Zr} in the undoped tetragonal ZrO_2 is equal to 1/3 of the Schottky defect formation free energy at the intrinsic E_{Fermi}, whereas the Schottky defect formation free energy (hence the $K_{Schottky}$) is further used to calculate the V_{Zr} concentration in the 3-mol % YSZ under the assumption of Y-doping independent $K_{Schottky}$. These results, in conjunction with the simulated cation migration barriers of 2–3 eV, predict apparent activation barriers of D_{Zr} in simulations (6.8–7.8 eV) greater than the experimental measurements for the 3-mol % YSZ (about 6 eV), as well as much smaller D_{Zr} than the experiments. These results indicate that for YSZ at low Y substitution, the model analysis based on a Y-independent Schottky reaction free energy would not be able to describe the experimental activation barriers, and hence there is a need to further examine how the Y substitution alters defect energetics, interactions, and migration barriers. Nonetheless, the effectiveness of the modeling results in describing the ionic transport for both the fast (H) and slow (cations) diffusing species in tetragonal bulk ZrO_2 demonstrates the utility of first principles calculations to quantify material defect chemistry and ionic transport under relevant temperature and humidity operating conditions and to allow predictions of the material transport properties under conditions not (yet) covered by experimental investigations.

V. CONCLUSIONS

In this work, a DFT-based modeling study was performed to investigate the defect thermodynamics and cation transport kinetics in bulk tetragonal ZrO_2 at various temperature and $P(O_2)$, $P(H_2)$, and $P(H_2O)$ pressure conditions. Guided by a bulk defect model which incorporates *ab initio* defect energetics and a three-dimensional random walk diffusion formalism, the effect of temperature, partial pressure of H_2 or O_2, and the humidity content, on the cation transport kinetics in bulk tetragonal ZrO_2 were assessed. In the defect thermodynamic modeling, the lattice phonon modeling revealed substantial supercell size dependence on vibrational free-energy contributions to the defect formation energy, particularly in the regime of high temperatures. The supercell-size convergence test results indicate that vibrational free energies of the defect formation can be reduced to 0.12 eV per defect when computations were performed using the $2\sqrt{2}a \times 2\sqrt{2}a \times 3c$ (288-atom) supercells. The results obtained from the defect thermodynamic modeling indicate that the apparent formation energy of $H_{Zr}(-3)$ is 0.5–0.7 eV lower than that of $V_{Zr}(-4)$, due to attractive interaction between $H_{int}(+1)$ and $V_{Zr}(-4)$ defects. Upon increasing the humidity content in both the $P(O_2)$-rich and $P(H_2)$-rich conditions, formation of the $H_{Zr}(-3)$ defect is promoted. The migration barriers of the $H_{Zr}(-3)$ versus $V_{Zr}(-4)$ are found to be comparable, i.e., 2.7eV versus 2.4 eV (3.0 versus 3.1 eV) with a difference of +0.3 eV (+0.1 eV) for the out-of-*ab*-plane migration (in-*ab*-plane migration).

Overall, the results obtained suggest that a few percent of $P(H_2O)$ in the temperature range 300–500 °C may be sufficient to cause a transition of bulk cation transport mechanism

from the $V_{Zr}(-4)$ transport to the $H_{Zr}(-3)$ transport, where the $H_{Zr}(-3)$ transport corresponds to dissociating a $H_{Zr}(-3)$ to form a $V_{Zr}(-4)$ and a $H_{int}(+1)$. Furthermore, another transition in the cation diffusion mechanism from the $V_{Zr}(-4)$ transport to the fully bound V_O-V_{Zr}-V_O carrier and the partially bound V_{Zr}-V_O carriers is predicted to occur at temperatures higher than 1573 K, where the vibrational free-energy contribution from anion vacancy formation activates the fully and partially bound Schottky defect transport mechanisms, despite the apparent activation barriers of $D_{Zr}(V_{Zr}$-$V_O)$ and $D_{Zr}(V_O$-V_{Zr}-$V_O)$ (about 6 eV) being larger than the 3.66–4.91 eV of $D_{Zr}(V_{Zr})$. On the other hand, the lower apparent activation energies of $D_{Zr}(V_{Zr})$ can result in higher diffusivities than the cation transport via the fully or partially bound Schottky defects at the temperatures below 1573 K, and above the $V_{Zr}(-4)$-to-$H_{Zr}(-3)$ cation transport transition temperature.

The modeling results also indicate that the most stable hydrogen defect species in the bulk tetragonal ZrO_2 is $H_{Zr}(-3)$, and its concentration is 4–6 orders magnitude higher than that of $H_{int}(+1)$. Nonetheless, the most active hydrogen transport occurs via the $H_{int}(+1)$ migration, rather than taking place through the stable $H_{Zr}(-3)$ defects, a fact due to the 1.2–1.4-eV difference in their migration barriers (0.2–0.4 eV versus 1.6 eV, respectively). The protonic transport rate in bulk tetragonal ZrO_2 is predicted to be several to a few tens order of magnitude higher than the bulk cation transport rate depending on the temperature. Overall, the results obtained highlight the importance of the coupling of the bulk cation transport kinetics with the dissolved H defect species at lower temperatures and with the cation-anion vacancy clusters at higher temperatures, and predict temperature dependent mechanistic transitions for the cation transport in tetragonal bulk zirconia.

ACKNOWLEDGMENTS

This research was supported by the National Energy Technology Laboratory's ongoing research in the area of property assessment of diffused interface modeling in solid oxide fuel cells. this research was executed through the NETL Research and Innovation Center's Solid Oxide Fuel Cell program. Research performed by Leidos Research Support Team staff was conducted under the RSS Contract No. 89243318CFE000003.

This work was funded by the Department of Energy, National Energy Technology Laboratory, an agency of the United States Government, through a support contract with Leidos Research Support Team (LRST). Neither the United States Government nor any agency thereof, nor any of their employees, nor LRST, nor any of their employees, makes any warranty, expressed or implied, or assumes any legal liability or responsibility for the accuracy, completeness, or usefulness of any information, apparatus, product, or process disclosed, or represents that its use would not infringe privately owned rights. Reference herein to any specific commercial product, process, or service by trade name, trademark, manufacturer, or otherwise, does not necessarily constitute or imply its endorsement, recommendation, or favoring by the United States Government or any agency thereof. The views and opinions of authors expressed herein do not necessarily state or reflect those of the United States Government or any agency thereof.

[1] J. Chevalier, L. Gremillard, A. V. Virkar, and D. R. Clarke, The tetragonal-monoclinic transformation in zirconia: lessons learned and future trends, J. Am. Ceram. Soc. **92**, 1901 (2009).

[2] H. Yokokawa, Y. Hori, T. Shigehisa, M. Suzuki, S. Inoue, T. Suto, K. Tomida, A. Kawakami, H. Sumi, M. Ohmori *et al.*, Recent achievements of nedo durability project with an emphasis on correlation between cathode overpotential and ohmic loss, Fuel Cells **17**, 473 (2017).

[3] H. Yokokawa, H. Kishimoto, T. Shimonosono, K. Yamaji, M. Muramatsu, K. Terada, K. Yashiro, and T. Kawada, Simulation technology on SOFC durability with an emphasis on conductivity degradation of ZrO_2-base electrolyte, J. Electrochem. Energy Convers. Storage **14**, 011004 (2017).

[4] A. H. Chokshi, Diffusion, diffusion creep and grain growth characteristics of nanocrystalline and fine-grained monoclinic, tetragonal and cubic zirconia, Scr. Mater. **48**, 791 (2003).

[5] M. Kilo, M. Weller, G. Borchardt, B. Damson, S. Weber, and S. Scherrer, Cation mobility in Y_2O_3- and CaO-stabilised ZrO_2 studied by tracer diffusion and mechanical spectroscopy, Defect Diffus. Forum **194-199**, 1039 (2001).

[6] J. Martinez-Fernandez, M. Jimenez-Melendo, A. Dominguez-Rodriguez, and A. H. Heuer, High-temperature creep of yttria-stabilized zirconia single crystals, J. Am. Ceram. Soc. **73**, 2452 (1990).

[7] K. Morita and K. Hiraga, Critical assessment of high-temperature deformation and deformed microstructure in high-purity tetragonal zirconia containing 3 mol.% yttria, Acta Mater. **50**, 1075 (2002).

[8] J. S. Hardy, J. W. Stevenson, P. Singh, M. K. Mahapatra, E. D. Wachsman, M. Liu, and K. R. Gerdes, Effects of humidity on solid oxide fuel cell cathodes, Report No. PNNL-24115, Pacific Northwest National Laboratory, 2015.

[9] Y. Dong, H. Wang, and I. W. Chen, Electrical and hydrogen reduction enhances kinetics in doped zirconia and ceria: i. grain growth study, J. Am. Ceram. Soc. **100**, 876 (2017).

[10] Y. Dong and I. W. Chen, Electrical and hydrogen reduction enhances kinetics in doped zirconia and ceria: II. mapping electrode polarization and vacancy condensation in YSZ, J. Am. Ceram. Soc. **101**, 1058 (2018).

[11] J. Pelleg, *Diffusion in Ceramics* (Springer, Cham, Switzeland, 2016).

[12] R. A. De Souza and M. Martin, Probing diffusion kinetics with secondary ion mass spectrometry, MRS Bull. **34**, 907 (2009).

[13] F. R. Chien and A. H. Heuer, Lattice diffusion kinetics in Y_2O_3-stabilized cubic ZrO_2 single crystals: a dislocation loop annealing study, Philos. Mag. A **73**, 681 (1996).

[14] Y. Dong, L. Qi, J. Li, and I. W. Chen, A computational study of yttria-stabilized zirconia: II. cation diffusion, Acta Mater. **126**, 438 (2017).

[15] Y.-L. Lee, Y. Duan, D. Morgan, D. C. Sorescu, H. Abernathy, and G. Hackett, Density funtional theory modeling of cation diffusion in bulk tetragonal zirconia, in *ACerS Ceramic*

Transactions (MS&T'18), edited by A. S. Bhalla *et al.* (John Wiley & Sons, New York, 2019), Vol. 266, pp. 95–110.

[16] G. Kresse and J. Hafner, Ab initio molecular dynamics for liquid metals, Phys. Rev. B **47**, 558 (1993).

[17] G. Kresse and J. Furthmüller, Efficient iterative schemes for ab initio total-energy calculations using a plane-wave basis set, Phys. Rev. B **54**, 11169 (1996).

[18] G. Kresse and D. Joubert, Phys. Rev. B **59**, 1758 (1999).

[19] J. P. Perdew, K. Burke, and M. Ernzerhof, Generalized Gradient Approximation Made Simple, Phys. Rev. Lett. **77**, 3865 (1996).

[20] H. J. Monkhorst and J. D. Pack, Special points for brillouin-zone integrations, Phys. Rev. B **13**, 5188 (1976).

[21] D. Broberg, B. Medasani, N. Zimmermann, A. Canning, M. Haranczyk, M. Asta, and G. Hautier, PyCDT: A python toolkit for modeling point defects in semiconductors and insulators, Comput. Phys. Commun. **226**, 165 (2018).

[22] S. P. Ong, W. D. Richards, A. Jain, G. Hautier, M. Kocher, S. Cholia, D. Gunter, V. L. Chevrier, K. A. Persson, and G. Ceder, Python materials genomics (pymatgen): A robust, open-source python library for materials analysis, Comput. Mater. Sci. **68**, 314 (2013).

[23] S. B. Zhang and J. E. Northrup, Chemical Potential Dependence of Defect Formation Energies in GaAs: Application to Ga Self-Diffusion, Phys. Rev. Lett. **67**, 2339 (1991).

[24] C. Freysoldt, J. Neugebauer, and C. G. Van de Walle, Electrostatic interactions between charged defects in supercells, Phys. Status Solidi B **248**, 1067 (2011).

[25] Y. Kumagai and F. Oba, Electrostatics-based finite-size corrections for first-principles point defect calculations, Phys. Rev. B **89**, 195205 (2014).

[26] A. Alkauskas, P. Broqvist, and A. Pasquarello, Defect Energy Levels in Density Functional Calculations: Alignment and Band Gap Problem, Phys. Rev. Lett. **101**, 046405 (2008).

[27] G. Miceli and A. Pasquarello, Energetics of native point defects in gan: a density-functional study, Microelectron. Eng. **147**, 51 (2015).

[28] J. L. Lyons and C. G. Van de Walle, Computationally predicted energies and properties of defects in GaN, Npj Comput. Mater. **3**, 12 (2017).

[29] J. Heyd, G. E. Scuseria, and M. Ernzerhof, Erratum: "Hybrid functionals based on a screened coulomb potential" [J. Chem. Phys. 118, 8207 (2003)], J. Chem. Phys. **124**, 219906 (2006).

[30] See Supplemental Material at http://link.aps.org/supplemental/10.1103/PhysRevResearch.3.013121 for the details of the computational modeling approach, the calculated DFT defect formation energies versus E_{Fermi}, the calculated ΔG_{form}(Defect) versus E_{Fermi} under the specified gas pressure and temperature conditions, the defect concentration and the intrinsic E_{Fermi} obtained from the defect model under the specified gas pressure and temperature conditions, the calculated migration barriers for the H_{Zr} hop at different charge states, and the modeled out-of-*ab*-plane $D_{\mathrm{Zr}}(V_{\mathrm{Zr}})$, $D_{\mathrm{Zr}}(V_{\mathrm{Zr}}$-$V_{\mathrm{O}})$, and $D_{\mathrm{Zr}}(V_{\mathrm{O}}$-$V_{\mathrm{Zr}}$-$V_{\mathrm{O}})$ versus inverse temperature in bulk tetragonal ZrO_2.

[31] Y.-L. Lee, Y. Duan, D. Morgan, D. C. Sorescu, H. Abernathy, and G. Hackett, Density functional theory modeling of a-site cation diffusion in bulk $LaMnO_{3\pm\delta}$ for solid oxide fuel cell cathodes, ECS Trans. **78**, 2797 (2017).

[32] G. Henkelman and H. Jónsson, Improved tangent estimate in the nudged elastic band method for finding minimum energy paths and saddle points, J. Chem. Phys. **113**, 9978 (2000).

[33] Y.-L. Lee, J. Holber, H. P. Paudel, D. C. Sorescu, D. J. Senor, and Y. Duan, Density functional theory study of the point defect energetics in γ-$LiAlO_2$, Li_2ZrO_3 and Li_2TiO_3 materials, J. Nucl. Mater. **511**, 375 (2018).

[34] A. Togo and I. Tanaka, First principles phonon calculations in materials science, Scr. Mater. **108**, 1 (2015).

[35] T. S. Bjørheim, E. A. Kotomin, and J. Maier, Hydration entropy of $BaZrO_3$ from first principles phonon calculations, J. Mater. Chem. A, **3**, 7639 (2015).

[36] T. S. Bjørheim, M. Arrigoni, D. Gryaznov, E. A. Kotomin, and J. Maier, Thermodynamic properties of neutral and charged oxygen vacancies in $BaZrO_3$ based on first principles phonon calculations, Phys. Chem. Chem. Phys. **17**, 20765 (2015).

[37] Y.-L. Lee and D. Morgan, Ab initio and empirical defect modeling of $LaMnO_3\pm\delta$ for solid oxide fuel cell cathodes, Phys. Chem. Chem. Phys. **14**, 290 (2012).

[38] R. J. D. Tilley, Chapter 7, in *Defects in Solids* (John Wiley & Sons, Hoboken, NJ, 2008).

[39] S. Beschnitt, T. Zacherle, and R. A. De Souza, Computational study of cation diffusion in ceria, J. Phys. Chem. C **119**, 27307 (2015).

[40] K. Momma and F. Izumi, VESTA: A three-dimensional visualization system for electronic and structural analysis, J. Appl. Crystallogr. **41**, 653 (2008).

[41] Y.-L. Lee, Y. Duan, D. Morgan, D. C. Sorescu, H. Abernathy, and G. Hackett, Density-functional-theory modeling of cation diffusion in bulk $La_{1-x}Sr_xMnO_{3\pm\delta}$ ($x = 0.0-0.25$) for solid-oxide fuel-cell cathodes, Phys. Rev. Appl. **8**, 044001 (2017).

[42] J. Rabone and P. Van Uffelen, DFT-based metadynamics simulation of proton diffusion in tetragonal zirconia at 1500K, J. Nucl. Mater. **459**, 30 (2015).

[43] C. Wagner, Die löslichkeit von wasserdampf in ZrO_2-Y_2O_3-mischkristallen, Ber. Bunsen-Ges. Phys. Chem. **72**, 778 (1968).

[44] S. Swaroop, M. Kilo, C. Argirusis, G. Borchardt, and A. H. Chokshi, Lattice and grain boundary diffusion of cations in 3YTZ analyzed using SIMS, Acta Mater. **53**, 4975 (2005).

[45] M. Kilo, G. Borchardt, B. Lesage, O. Kaıtasov, S. Weber, and S. Scherrer, Cation transport in yttria stabilized cubic zirconia: 96Zr tracer diffusion in $(Zr_xY_{1-x})O_{2-x/2}$ single crystals with $0.15 \leqslant x \leqslant 0.48$, J. Eur. Ceram. Soc. **20**, 2069 (2000).